IOWA STATE UNIVERSITY
Digital Repository

Retrospective Theses and Dissertations

Iowa State University Capstones, Theses and Dissertations

2007

Structural and electronic properties of nanocrystalline silicon thin film solar cells fabricated by hot wire and ECR-plasma CVD techniques

Kamal Kumar Muthukrishnan
Iowa State University

Follow this and additional works at: https://lib.dr.iastate.edu/rtd

 Part of the Electrical and Electronics Commons

Recommended Citation
Muthukrishnan, Kamal Kumar, "Structural and electronic properties of nanocrystalline silicon thin film solar cells fabricated by hot wire and ECR-plasma CVD techniques" (2007). *Retrospective Theses and Dissertations*. 15518.
https://lib.dr.iastate.edu/rtd/15518

This Dissertation is brought to you for free and open access by the Iowa State University Capstones, Theses and Dissertations at Iowa State University Digital Repository. It has been accepted for inclusion in Retrospective Theses and Dissertations by an authorized administrator of Iowa State University Digital Repository. For more information, please contact digirep@iastate.edu.

www.manaraa.com

Structural and electronic properties of nanocrystalline silicon thin film solar cells fabricated by hot wire and ECR-plasma CVD techniques

by

Kamal Kumar Muthukrishnan

A dissertation submitted to the graduate faculty

in partial fulfillment of the requirements for the degree of

DOCTOR OF PHILOSOPHY

Major: Electrical Engineering

Program of Study Committee:
Vikram L. Dalal, Major Professor
Gary Tuttle
Rana Biswas
Joseph Shinar
Alan Constant

Iowa State University

Ames, Iowa

2007

Copyright © Kamal Kumar Muthukrishnan, 2007. All rights reserved.

www.manaraa.com

UMI Number: 3259460

UMI

UMI Microform 3259460

Copyright 2007 by ProQuest Information and Learning Company.
All rights reserved. This microform edition is protected against
unauthorized copying under Title 17, United States Code.

ProQuest Information and Learning Company
300 North Zeeb Road
P.O. Box 1346
Ann Arbor, MI 48106-1346

www.manaraa.com

TABLE OF CONTENTS

ACKNOWLEDGEMENTS iv

ABSTRACT v

CHAPTER 1: ABOUT THIS RESEARCH 1
1.1 Research Motivation 1
1.2 Introduction 2
1.3 Research Objective 4

CHAPTER 2: LITERATURE SURVEY 6
2.1 Growth Models for Silicon Thin Film Deposition 6
2.2 Nanocrystalline Material and Growth Parameters 10
2.3 Hot Wire or the Catalytic CVD Process 22
2.4 Solar Cells with Nanocrystalline Intrinsic Layers Fabricated by HWCVD 26

CHAPTER 3: EXPERIMENTAL SET-UPS 31
3.1. Device Fabrication 31
3.1.1. Combined Hot Wire ECR PECVD Reactor 31
3.1.2. ECR Deposition 34
3.2. Design of the Solar Cell 35
3.3 Thin Film Characterization Techniques 37
3.3.1. Thickness Measurement 37
3.3.2. Raman Spectroscopy 38
3.3.3. X-Ray Diffraction 39
3.4. Device Characterization Techniques 41
3.4.1. I-V Characterization 41
3.4.2. Quantum Efficiency Measurement 44
3.4.3. Capacitance-Voltage (CV) Measurements 46
3.4.4. Diffusion Length of Minority Carriers 47
3.4.5. Device Contacts 51
3.5. Plasma Characterization by Quadruple Mass Spectroscopy 51
3.6. MESA Etching Technique to Pattern Device Contacts 53
3.6.1. Preclean 53
3.6.2. Image Reversal Photoresist 53
3.6.3. P+ Layer Etch 53
3.6.4. Photoresist Removal 53

CHAPTER 4: RESULTS AND DISCUSSION 54
4.1. Effect of Hot Wire CVD Parameters on Grain Size and Orientation 54
4.1.1. Effect of the Hydrogen Dilution 54

www.manaraa.com

4.1.2. Effect of Substrate Temperature 56
4.1.3. Effect of Chamber Pressure 57
4.2. Effect of Helium Addition in HWECR and HWCVD 59
4.2.1. Effect of the Incident Microwave Power 59
4.2.2. Effect of Helium Dilution Ratio 61
4.2.3. Effect of Plasma Ions in Combined Hot Wire and ECR CVD Depositions 62
4.3. Detection of Growth Radicals Using Quadruple Mass Spectrometer 64
4.4. Process and Design Optimization of Nanocrystalline Solar Cell Devices 67
4.4.1. The MESA Etch Technique 67
4.4.2. Effect of Post Thermal Annealing 69
4.4.3. Effect of Boron Grading 70
4.5. Results on Nanocrystalline Solar Cells 72
4.5.1. Why Transition Region for High Efficiency Devices? 72
4.5.2. Effect of Filament Temperature 74
4.5.3. Effect of Chamber Pressure 76
4.5.4. Results on Devices from Combined Hot Wire and ECR CVD Techniques 78

CHAPTER 5: CONCLUSIONS 80

FUTURE RESEARCH DIRECTIONS 83

REFERENCES 84

www.manaraa.com

ACKNOWLEDGEMENTS

First and foremost, I would like to thank my major professor Dr. Vikram L. Dalal for his constant support and guidance throughout this research. Without his encouragement and invaluable suggestions, this work would not have seen the light of the day. Next I would like to thank Dr. Gary Tuttle, Dr. Rana Biswas, Dr. Joseph Shinar and Dr. Alan Constant for serving in my POS committee and reviewing my work carefully.

My sincere thanks to Max Noack, for his constant help with several experimental set-ups and for many useful discussions. Next I would like to thank Nanlin, Kay, Durga, Puneet, Debju, Ted and Atul for their help with my device depositions. Thanks to Satya, Vishwas, Cole, Diana and Leah for their help with device measurements. I would also like to thank the MRC graduates Andy, Mattring, Jason and Jarrod for many interesting and useful discussions in the past.

My thanks are due to Jane Woline and Pam Myers for their constant help with many paper works and graduate college procedures. I would like to thank all my friends at ISU for making my graduate studies the most memorable one. Particularly I would like to thank Venkat, Vivek, Murali, Anil, Sudershan and Mothivel for their many useful suggestions on my thesis.

I would like to thank my parents, sister, nephew and my brother-in-law for their moral support and constant encouragement to finish my work.

Finally but certainly not the least of all, I would like to thank Catron Solar Energy Foundation and NREL, for financially supporting this work.

www.manaraa.com

ABSTRACT

Nanocrystalline silicon has become the material of interest recently, for solar cell applications and also in the fabrication of thin film transistors. The material contains crystalline grains surrounded by amorphous tissues and when used as intrinsic layer in solar cell devices, greatly enhances the device stability against the light induced degradation which is a critical problem with amorphous silicon solar cells. The conventional PECVD techniques used for the deposition of high efficiency devices have a major drawback of very low growth rates. This project deals with a systematic study of structural and electronic properties of nanocrystalline Si:H films and devices fabricated using a relatively new technique called the Hot Wire CVD (HWCVD). In addition, we study the influence of ions on the crystalline ratio, grain size and orientation of the nanocrystalline films. Our apparatus allows us to add plasma ions separately from the primary growth process, which is growth using only radicals that are generated by the thermal dissociation of silane and hydrogen at the hot wire. In this way, we have also deposited the first ever nanocrystalline silicon solar cells by the combined HWCVD and Electron Cyclotron Resonance (ECR) PECVD technique.

While hot wire deposition of nanocrsytalline Si:H has been studied in the past, virtually all previous work utilized a close-proximity hot wire deposition condition that creates a varying temperature profile during deposition because of the intense heating of the growing film due to radiation from the filament. In contrast, in this work, we use a remote filament to minimize sample heating, a conclusion verified by experimental measurements of surface temperatures during growth conditions. We have found that low energy ion bombardment, by either inert (helium) or reactive (hydrogen) ions significantly helps in

www.manaraa.com

crystallization of the film. We also systematically study the influence of hydrogen dilution on grain size and grain orientation of the film. It is found that higher hydrogen dilution suppresses the <220> grains and leads to more random nucleation. It is found that <220> orientation is the thermodynamically preferred growth direction and <111> grains are created due to random nucleation which is enhanced by increasing the ion bombardment from the plasma source. We have also studied the fragmentation pattern of silane in ECR PECVD using a quadruple mass spectrometer. The study revealed the dominant radicals in both nc-Si and a-Si depositions for varying power and chamber pressures.

In the second part of this work, we focus primarily on the fabrication and analysis of the electronic properties of solar cells using nanocrystalline intrinsic layers. Apart from measuring the regular I-V characteristics and quantum efficiency, we investigate the critical device properties such as the defect densities in the intrinsic layer and the diffusion length of the minority carriers. By correlating the device results with the structural properties of the films, we are able to conclude that the maximum diffusion length and the minimum defect density can only be attained by depositing the intrinsic layers that are close to the transition to amorphous phase. Although few studies have been done on this transition regime of the deposited films, most of them have concentrated only on the film properties such as conductivity ratios and crystalline fractions. This work clearly describes why transition region is ideal for the fabrication of high efficiency solar cells and what are the critical deposition parameters that are involved in their design.

www.manaraa.com

CHAPTER 1: ABOUT THIS RESEARCH

1.1 Research Motivation

Solar cells with nanocrystalline silicon intrinsic layers are unique photovoltaic devices because of their prolonged stability against light induced degradation and improved carrier collection at higher wavelengths. It is also much cheaper to deposit when compared to that of pure crystalline silicon. These properties have made the nanocrystalline silicon to be extensively used in the fabrication of high efficiency thin film solar cells and also in thin film transistors. However since this material has an indirect bandgap and a lower absorption co-efficient, the intrinsic layer of the solar cell has to be at least several μm thick for effective absorption which demands process technologies with high growth rates.

Conventional PECVD techniques have been used to fabricate solar cells with good efficiency. For a single junction nanocrystalline solar cell, efficiencies greater than 10% has been obtained [1], but at a very low growth rate. The other promising technique is the HWCVD which yields much higher growth rates at low substrate temperatures. This technique has the process capability to switch to very low temperatures that are ideal for deposition on flexible substrates, without sacrificing much growth rate. The combined advantages of the nanocrystalline silicon material and its fabrication using the hot-wire CVD technique are the major motivating factors for the present research work and has also led to several novel research in this area.

Recently Klein et. al. [2] reported a record efficiency of 9.4% for nanocrystalline solar cell with intrinsic layer fabricated by HWCVD. The current trend is to fabricate the absorber layers in the solar cells in a region close to the transition to amorphous phase in

www.manaraa.com

order to get maximum efficiency. Although much work has been done on films fabricated in this regime to explore its structural properties, there are virtually no reports on the electronic properties such as diffusion length and defect densities of the material in actual devices to explain the enhanced efficiency in the transition region.

In this work we first study the structural and electronic properties of nanocrystalline thin films under controlled deposition conditions, both in the presence of plasma ions and hot wire radicals. Then we systematically study the variation in the fundamental electronic properties of thin film solar cells with absorber layers of varying crystalline ratios. By correlating these electronic properties with the structural properties of the absorber layers, we are able to find out the fundamental cause for obtaining high efficiencies at the transition region and also the optimal deposition conditions.

1.2 Introduction

Solar energy remains as one of the most promising renewable source of energy. Active research has been carried over for the past few decades to improve the conversion efficiency of the photovoltaic devices. The state of the art amorphous silicon solar cells have an efficiency of 11%, higher than that of their nanocrystalline counterparts, but amorphous material has its own disadvantages, the critical problem being the Staebler Wronski effect, which is the device degradation under prolonged exposure to sunlight.

Alan Fahrenbruch and Richard Bube quoted in their book that *" There are three main areas in which a commercially viable solar cell must excel: 1) cost, (2) efficiency, and (3) operating lifetime. Clearly these are not independent, but are mutually related"* [3]. For example, if we consider amorphous silicon solar cell, the deposition cost is comparatively

www.manaraa.com

low and the efficiency is much higher, but the operating lifetime with high efficiency is very low. On the other hand, the operating lifetime of a nano-crystalline device is long, but the device has lower efficiency and also much more expensive to deposit because of the low growth rates involved in the conventional techniques. Here arises the need for a good quality material that will yield a high efficiency solar cell and also an optimum technique to deposit the material at a minimum cost.

Although amorphous silicon (a-Si:H) solar cells are more common in the industrial solar cell technology, they don't have much efficient absorption at longer wavelengths. An alternative is to use a-(Si,Ge):H, with a smaller bandgap than a-Si:H, but this material has poorer properties than a-Si:H and is also more unstable than a-Si:H [4]. The nanocrystalline silicon which consists of crystalline grains embedded in an amorphous matrix combines the advantages of both the a-Si:H and extended absorption of the crystalline silicon at long wavelengths. In addition to this property, this material has very good stability against degradation under extended light soaking [5].

Plasma enhanced chemical vapor deposition (PECVD) is the commercially established standard process for the deposition of these materials [6, 7]. In view of higher deposition rates over very large areas there is always much scope for other deposition techniques. The Hot-wire chemical vapor deposition (HWCVD) or the Catalytic chemical vapor deposition (CAT-CVD) has recently received much attention in this regard [8, 9]. The inherent advantages of HWCVD are,

- very high deposition rate with a solid potential for upscaling [10]
- relatively simplified chemistry of the deposition process due to the absence of plasma and ions [4]

www.manaraa.com

- the gas utilization efficiency is 5-10 folds higher than that of PECVD which considerably decreases the consumption of raw materials and improves the overall growth rate [11]
- the film and the substrate are both free from plasma damage or charge-induced damage which is a huge advantage in case of ultra-large scale integrated circuit (ULSI) fabrication that are extremely sensitive to the charge-induced damage [11]

These characteristics have made HWCVD as one of the alternative techniques in solar cell fabrication and also in the electronics industries for TFT fabrications. Since this deposition technique is free from the plasma ions, it is used in the fabrication of photoconductive layers for copy machines and in the automobile industry for surface coating of metal substrates. Due to its high gas barrier ability and low temperature processing, it is also used in biotechnology for the surface passivation of biosensors [11]. Thus hot-wire CVD has become more diverse in its application due to its inherent advantages over the other techniques.

This work focuses entirely on analyzing the structural and electronic properties of nanocrystalline silicon thin films and devices deposited by the hot-wire technique and on studying the impact of ions on the properties of nc-Si:H films and devices grown by HWCVD.

1.3 Research Objective

The main objective of this research is to determine the deposition conditions favoring the fabrication of high efficiency nanocrystalline silicon solar cells and to investigate the effect of these conditions on some of the fundamental electrical characteristics of the device

www.manaraa.com

that are critical to improve its efficiency. In the first part of the work, we study the effect of hot wire deposition parameters on the structural properties of nanocrystalline films deposited on stainless steel substrates. The characterization techniques that we use for our analysis are Raman Spectroscopy, X-ray diffraction and UV/NIS/NIR spectrophotometry. We explore the variation of grain size and orientation in the nanocrystalline thin films, influenced by the hot wire radicals under different growth conditions. In addition we also study the variation of these structural properties in the presence of plasma ions, by combining both hot wire CVD and electron cyclotron resonance PECVD techniques. This allows us to clearly distinguish the influence of plasma ions from the hot wire radicals.

In the second part, we fabricate solar cell devices with nanocrystalline intrinsic layers by systematically varying the hot wire deposition parameters and probe the electrical characteristics of the device. Apart from the I-V characteristics, the other fundamental characteristics explored are the quantum efficiency, diffusion length of minority carriers and the C-V characteristics. We then correlate the structural properties that we studied on the films with the electrical properties of the final devices to determine the optimum growth conditions in fabricating high efficiency nanocrystalline silicon solar cells.

www.manaraa.com

CHAPTER 2: LITERATURE SURVEY

2.1 Growth Models for Silicon Thin Film Deposition

The standard growth model describing both PECVD and HWCVD depositions is the Matsuda, Gallagher, and Perrin model, otherwise known as the MGP model [12, 13, 14]. According to this model, the excess hydrogen on the surface is abstracted by the silyl radicals that are generated primarily by dissociation of silane. This creates a several vacant sites on the surface of the growing film. The fresh silyl radicals that have very low sticky co-efficient are mobile and diffuse over the film surface to reach the vacant sites and bond with the silicon atom. Thus this model primarily states that the growth of the thin film is dependant upon the abstraction of hydrogen by the silyl radicals and also their surface diffusion to vacant sites.

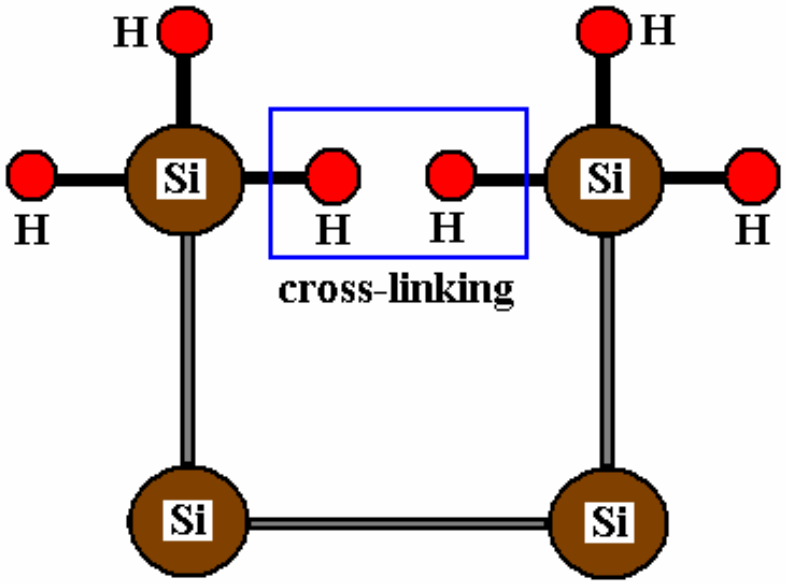

Figure 2.1: Schematic representation of the MGP model

www.manaraa.com

The model also states that the cross linking between adjacent hydrogen atoms of the silyl radicals can me a mode of abstraction. This is illustrated in Figure 2.1. However the model does not address the role of hydrogen ions in plasma in improving the structural properties of the material.

Both Robertson and Dalal explained the role of hydrogen ions in the growth model [15,16]. Dalal stated that the excess hydrogen atoms on the surface are broken and abstracted by the incoming plasma hydrogen ions rather than their abstraction by the silyl radicals [16]. Dalal also explained the role of inert ions like helium in the plasma during the growth process. He stated that the helium ions can easily break the bonded hydrogen atoms in the surface creating new dangling bonds. The hydrogen ions on the other hand can penetrate the surface to remove the weakly bonded hydrogen atoms from subsurface. Hydrogen ions also improve the radical selectivity by increasing the concentration of silyl radicals during the deposition. Miyazaki et al. showed the influence of hydrogen ions in changing the a-Si film structure after H_2 plasma treatment using Raman scattering spectra [17].

Robertson used thermodynamics and reaction kinetics to propose a model for the material growth with ion bombardment [15]. According to his model, the hydrogen ions react with the weakly bound surface hydrogen by forming a H_2^* complex. This complex has a lower free energy transition state than a single atom and this drives the complex to diffuse through the film easily to the surface.

In one of his other works, Dalal explained how hydrogen ions help in homogenizing the growing film surface and prevent defect incorporation [18]. The presence of different radicals in the plasma can make a growing surface very non-homogenous with passive Si-H bonds and active sites as shown in Figure 2.2.

www.manaraa.com

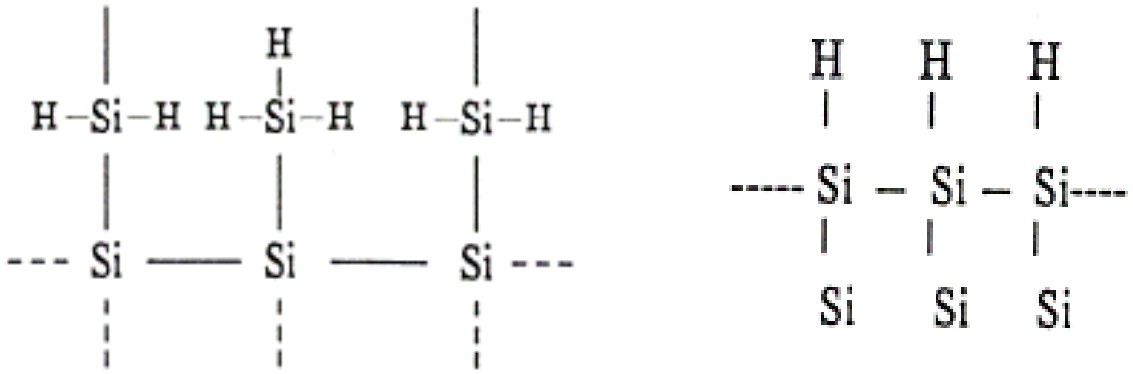

Figure 2.2: Surface homogenization by the hydrogen ions [18]

When these Si-H bonds are buried during subsequent deposition, they can potentially lead to the formation of voids in the material. The hydrogen ions attach themselves to the active sites making the surface very homogeneous and in the next stage, all the surface bound hydrogen atoms are removed by the incoming hydrogen ions.

Nickel and Jackson studied the role of hydrogen in relaxing the hydrogenated amorphous silicon (a-Si:H) network by exposing the material to hydrogen plasma [19]. As shown in the Figure 2.3, hydrogen from the plasma targets a weak Si-Si bond in the network. The strained bond is broken into two Si-H bonds thus relaxing the network locally. But this strain is now passed on to the adjacent Si-Si bond as shown in the figure. Thus, according to Nickel et al. during hydrogenation, the average network strain in the amorphous network remains unchanged, but the average strain energy per bond, represented by Urbach energy decreases to a minimum. Morral et al. explained the four staged transformation of amorphous to crystalline material induced by the hydrogen ions [20]. In the first stage which is the incubation phase, the hydrogen ions change the dense amorphous network in to a porous

www.manaraa.com

layer which acts as a substrate for the crystallite nuclei that from during the nucleation phase. The nucleation is followed by the growth phase during which individual crystalline grains originate from the nuclei and the final stage is the steady state phase when the growth of the crystallites becomes stable.

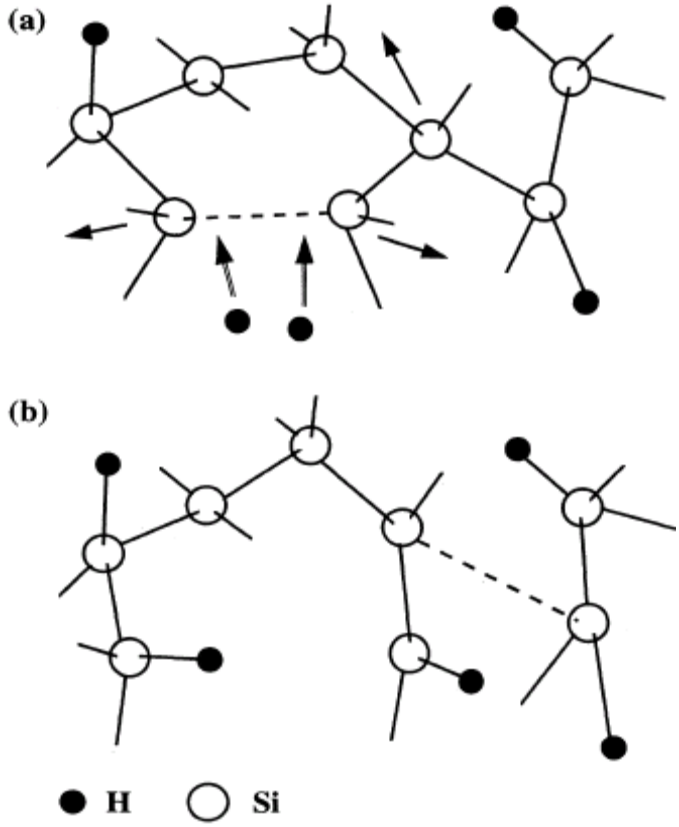

Figure 2.3: Role of H ions in relaxing a a-Si:H network [19]

In a very recent work, Sriraman et. al. clearly explained the hydrogen mediated crystallization by post treating hydrogenated amorphous silicon with an hydrogen plasma [21].They stated that the hydrogen diffuses into the amorphous matrix and inserts into strained Si-Si bonds thus forming hydrogen centered Si-H-Si bond. These hydrogen later breaks away from these intermediate bonds which undergo re-arrangement to form a more

www.manaraa.com

ordered structure. They concluded that the bond angles and the bond lengths in the final structure is close to that of crystalline silicon.

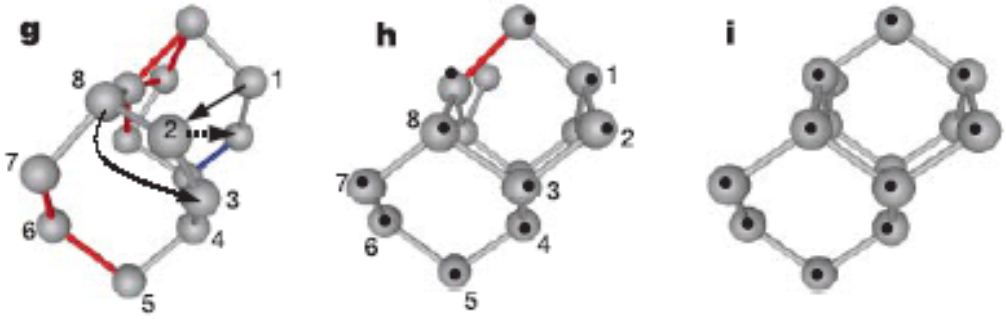

Figure 2.4: Structural re-arrangements in amorphous silicon (g) resulting in a more ordered material (h) whose bond lengths and angles are close to that of a crystalline material (i). [21]

2.2 Nanocrystalline Material and Growth Parameters

Nanocrystalline silicon has received much attention recently, particularly for solar cell applications because of its enhanced stability against light induced degradation and higher absorption at longer wavelengths.

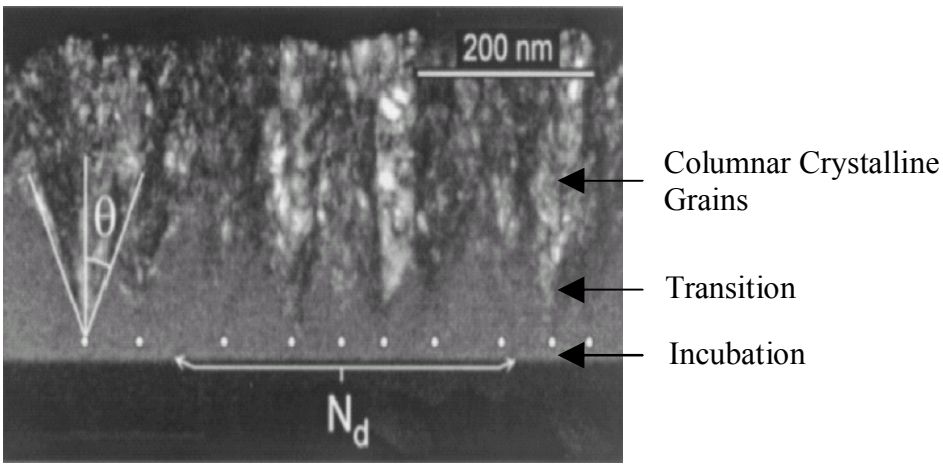

Figure 2.5: TEM picture showing nanocrystalline silicon growth [22]

www.manaraa.com

As shown in Figure 2.5, the material has a unique structure of crystalline grains surrounded by grain boundaries composed of amorphous tissues which are passivated by hydrogen ions during the growth process. All nanocrystalline material deposition is started with a thin amorphous layer which acts as a incubation layer or the substrate for the nuclei of crystalline grains. The nucleation density (N_d) and the transition to crystalline phase strictly depend upon the deposition conditions. Levi et al. reported in their work that the incubation layer thickness remains the same for most of the deposition conditions but the thickness of the transition region varies drastically [23]. When conditions favor the formation of crystalline phase, the transition layer thickness decreases significantly as shown in Figure 2.6.

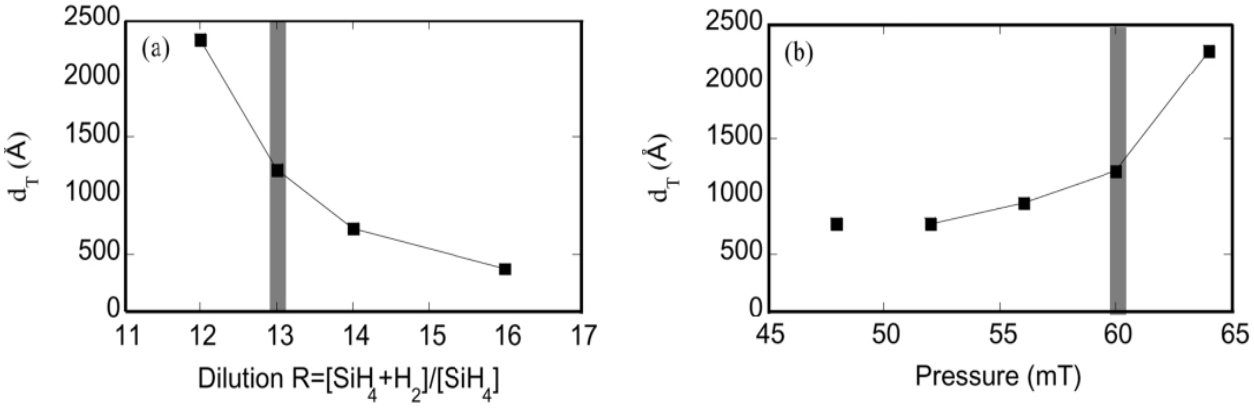

Figure 2.6: Effect of hydrogen dilution and chamber pressure on the thickness of transition layer [23]

The grain boundaries surrounding the crystalline grains also play a important role in the material characteristics, since they are the barriers to carrier transport in the material. Takakura and Hamakawa and have shown the electronic potential distribution for the grain boundaries in a nc-Si matrix [24]. The electron density simulation as shown in Figure 2.7,

www.manaraa.com

reveals a kink at the grain boundary and they conclude that the peak and valley found in the grain boundaries act as a minority carrier sink and their strength is dependant upon the defect density Ngb.

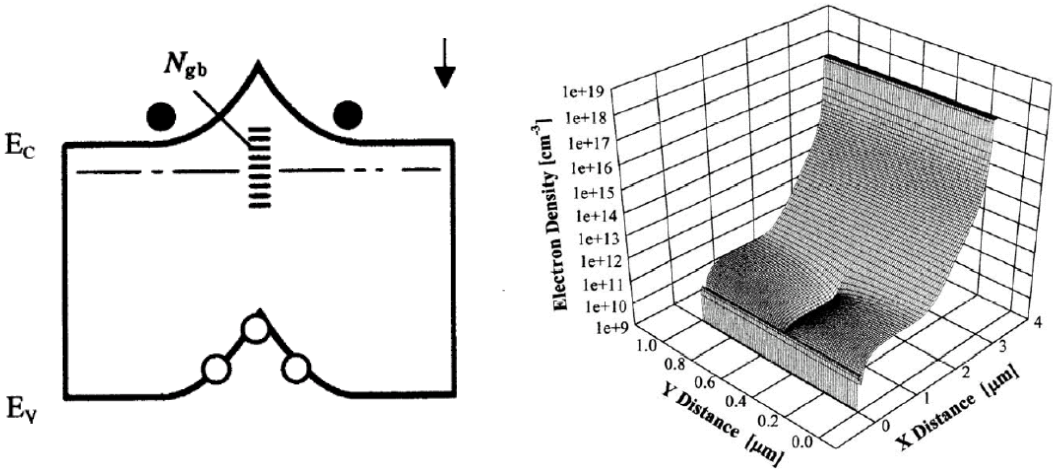

Figure 2.7: Electronic potential and electron density in grain boundary [24]

Keppner et al. have showed in their work that the grain boundaries can be passivated by a high concentration of hydrogen [25]. Biswas and Pan postulated that the grain boundary is highly strained with distorted bonds and bond angles [26,27]. Through molecular dynamics simulations they showed that the H distribution in nc-Si is highly inhomogeneous. The simulation results revealed that the bulk of the H-density is concentrated in the grain boundaries wherein they passivate the dangling bonds and also the strained bonds.

Liu et al. [28] explained the different transport mechanisms in nanocrystalline silicon by measuring the dark conductivity for samples of varying crystallinity and correlating it with temperature variations. The energy band diagram of a nanocrystalline silicon is shown in Figure 2.8, considering the presence of thick amorphous tissues along the grain boundaries.

www.manaraa.com

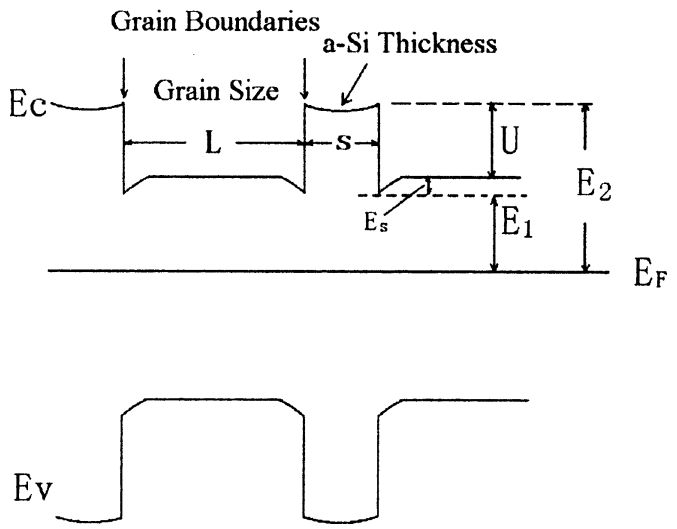

Figure 2.8: Energy band diagram of a nanocrystalline silicon thin film [28]

Based on their conductivity measurements, Liu et al. concluded that for samples with low crystalline fraction, the transport of carriers occur by thermionic emission at room temperature. When the crystalline fraction of the material increases, the carriers can effectively tunnel through the potential barriers. The other type of transport mechanism that occurs at low temperatures for samples of low crystallinity is the carrier hopping between localized states and conduction through the tail states adjacent to the conduction and valence bands.

The growth of good quality nanocrystalline silicon (nc-Si) films using the hot-wire technique is a little complicated when compared to amorphous silicon. This is because individual parameters like hydrogen dilution profiling, silane concentration, substrate temperature, chamber pressure, filament temperature, the number of filaments and the filament-substrate distance play a very critical role in the structural properties of the deposited film by altering the ratio of crystalline to amorphous phase.

www.manaraa.com

Klein et al. concluded that the hydrogen desorption during the growth process increases with substrate temperatures above 300C leading to insufficient grain boundary passivation and hence increased defect densities [29]. Schropp has shown in his work that if the substrate temperature is made too high, the crystalline fraction and the grain sizes are greatly enhanced but this happens at the expense of material quality. The material becomes porous at very high temperatures and this finally leads to in-diffusion of atmospheric gases including oxygen [30]. The infrared absorption spectra in Figure 2.9, shows the influence of substrate temperature on material property [31]. The SiO peak which is an indication of the porous material can be prominently seen at higher temperatures. Also at lower temperatures, the SiH stretching mode at 2000cm^{-1} increases at the expense of the doublet at 2100cm^{-1} indicating a more compact structure.

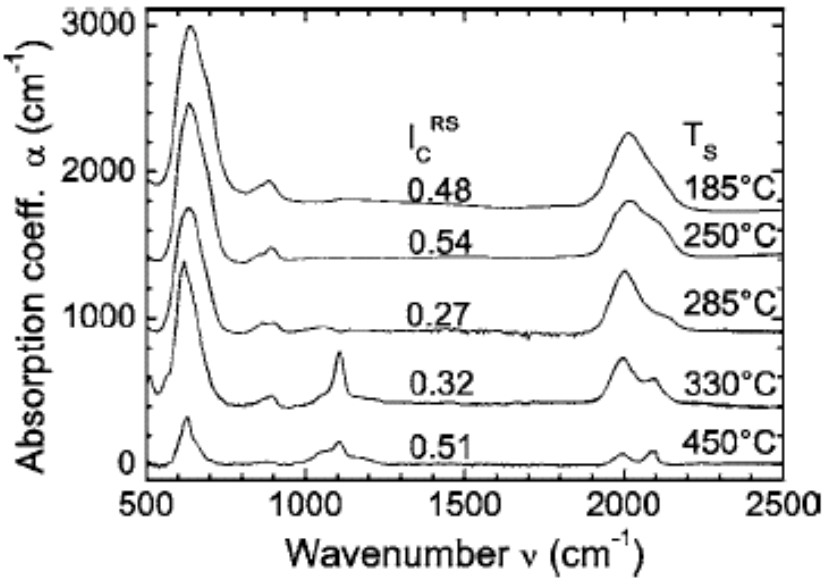

Figure 2.9: Infrared absorption spectra of μc-Si films prepared with different substrate temperatures [31]

www.manaraa.com

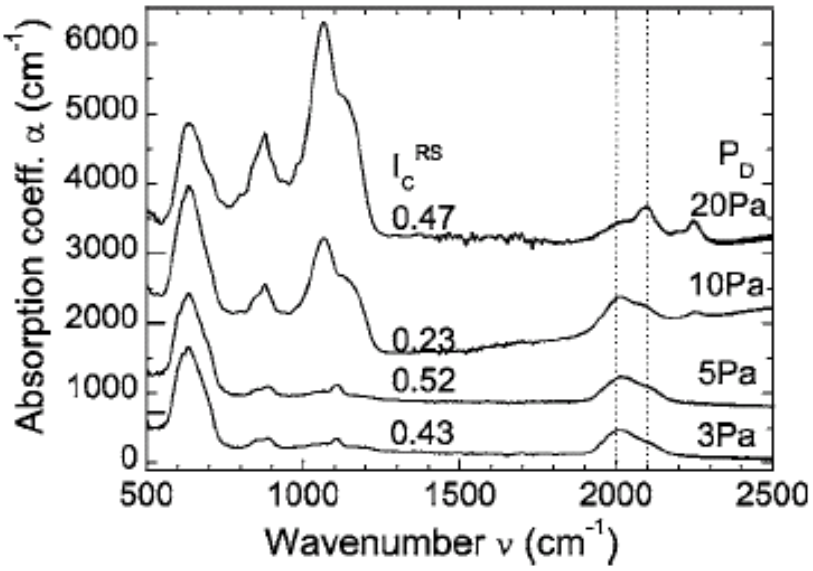

Figure 2.10: Infrared absorption spectra of μc-Si films prepared with different substrate temperatures [31]

The absorption spectra indicates prominent SiO peak at ~1050cm-1 and the oxygen related SiH stretching mode at 2250 cm-1 at very high pressure which is a very good indication of porous material. Further the SiH2 scissor mode is evident at higher pressure which is a strong indication of increasing hydrogen content in the material. The results shown in Figure 2.10 prove that very high pressure is detrimental to the growth of good quality nanocrystalline films.

One of the key components in obtaining a good crystalline material is the hydrogen dilution. Niikura et al. have studied the effect of hydrogen dilution on the crystalline fraction and deposition rates at different regimes of chamber pressure [32]. As shown in Figure 2.11, increasing the hydrogen dilution in the deposition gas mixture, increases the crystalline fraction of the film in both high pressure (HP) and low pressure (LP) regimes. The interesting

www.manaraa.com

result from the plot is the transition from amorphous to crystalline phase, which occurs only at a hydrogen dilution of over 90% when operating in the high pressure regime.

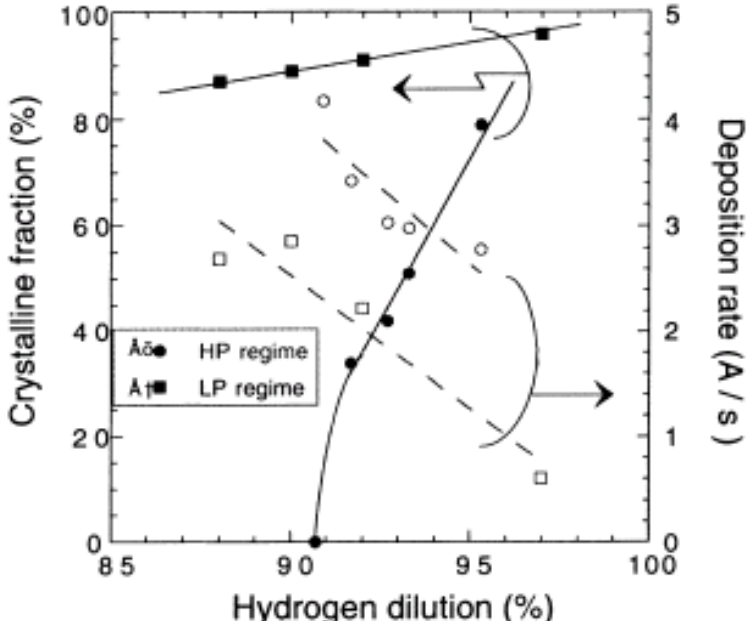

Figure 2.11: Effect of hydrogen dilution and pressure regimes [32]

It can also be seen that the deposition rate decreases with increase in hydrogen dilution with the minimal rates occurring in the low pressure regime. The silane concentration has the opposite effect on the crystalline fraction. The crystallinity of the film decreases with increase in silane content of the gas mixture. By increasing the filament temperature and the substrate temperature, the crystallinity region can be prolonged even with increase in the silane concentration. Klein et al. showed the effect of silane concentration on the crystalline fraction of the material by measuring the Raman intensity in the samples as shown in Figure 2.12 [31]. It is clear from the plot that the transition to amorphous phase occurs at much lower silane concentrations when the chamber pressure is increased. J. Lossen et al. reported that increasing the filament temperature increases the

www.manaraa.com

deposition rate and also the crystallinity of the film but this leads to deterioration in the film quality [33].

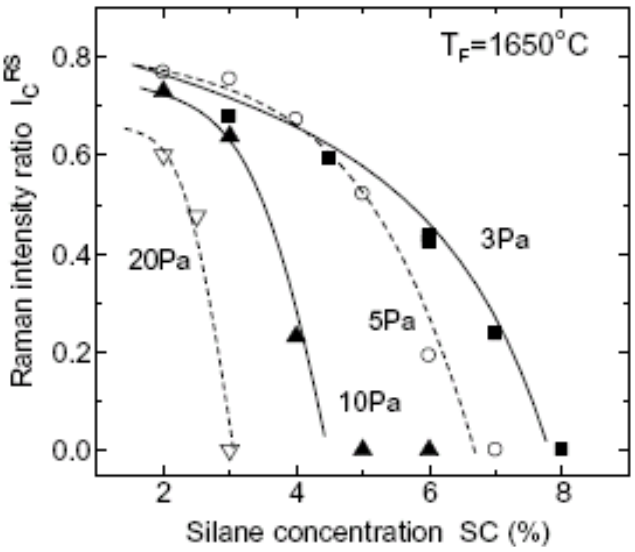

Figure 2.12: Effect of chamber pressure on the crystalline fraction of the deposited film [31]

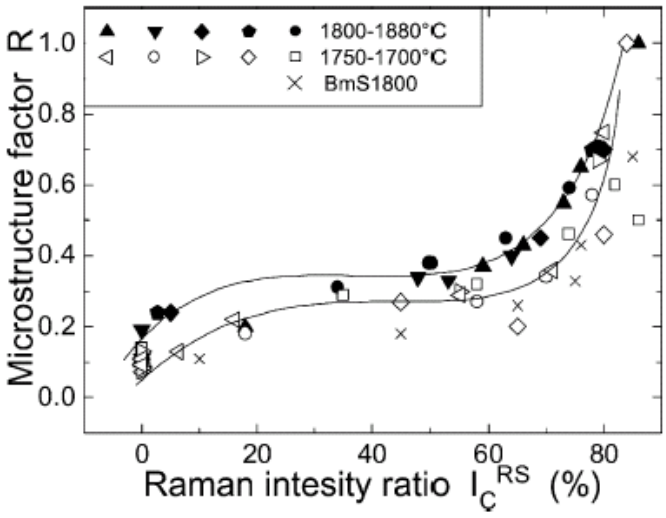

Figure 2.13: Microstructure factor (R) Vs Crystallinity ratio [33]

www.manaraa.com

As shown in the Figure 2.13, at elevated filament temperatures, the microstructure factor of the film is also high, which is a clear indication of a porous material. They also concluded that by decreasing the filament-substrate distance and the filament surface area, increased deposition rates can be achieved without sacrificing the material properties.

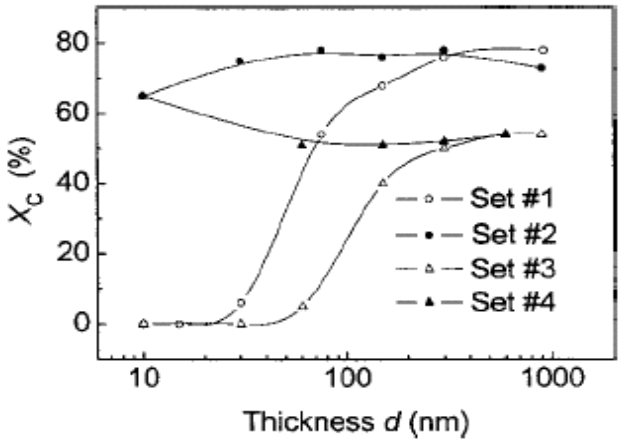

Figure 2.14: Depth profiles in X_c for films: set 1 (R=95%), set 2 (R =98%/97%/96%/95%), set 3 (R=90%), and set 4 (R=98%/91%/90.5%/90%). [34]

Gu et al. have explored the importance of hydrogen dilution profiling (HDP) during the deposition of nanocrystalline silicon [34]. It was concluded that the uniformity of the crystallinity can be controlled by the HDP approach and by selecting a proper HDP model its possible to obtain the desired material properties of the depositing film. From Figure 2.14, it can be seen that by maintaining a high hydrogen dilution during the growth of incubation layer, the thickness of the non-uniform transition region can be considerably reduced. This is because, the increased hydrogen dilution enhances the nuclei density and restricts the incubation layer to within 10nm thus promoting the material compactness and structural uniformity. They have also explored the compactness of the film using their HDP approach. The FTIR spectra for the set of samples at various hydrogen dilution is shown in Figure 2.15.

www.manaraa.com

Sample H101 which is with the highest R (98%) shows a strong peak at 1070 cm^{-1}, a strong indication for a film with internal voids. On the hand samples H153 and H185 which had a initial R of 98% and were later profiled by decreasing the dilution showed no signs or peaks of very less magnitude at 1070 cm^{-1}, even after exposing these films to atmosphere for 2 and 300 days. Also the structure factor evaluated using the peaks at 2000cm^{-1} and 2090cm^{-1} were very low for H153 and H185 indicating a more compact structure. Thus by a proper HDP method, the stability of the film can be improved to a great extent.

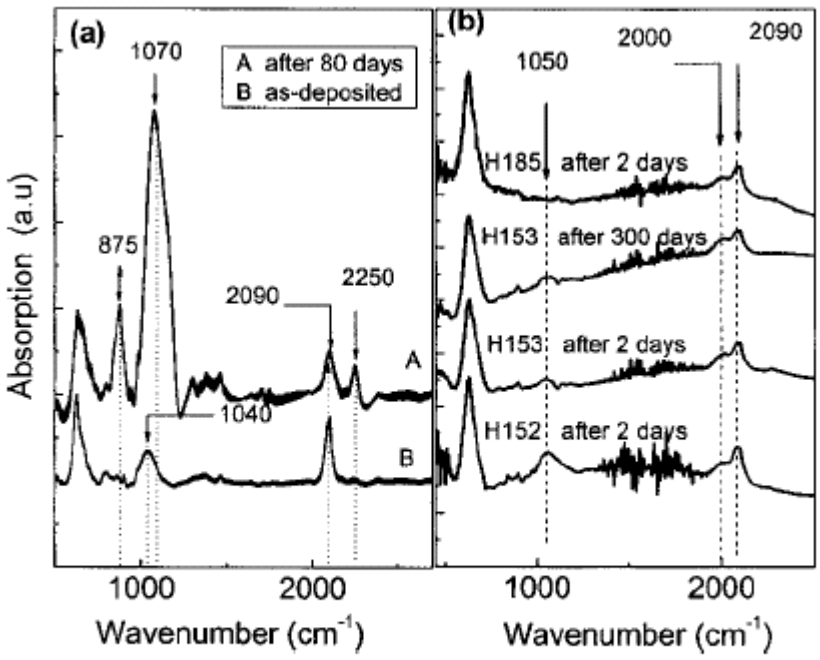

Figure 2.15: FTIR for (a) sample H101, (b) H152 (R=95%), H153 (R =98%/95%), H185 (R=98%/97%/96%/95%). [34]

Very few studies have been done on the variation of grain sizes with deposition parameters. Nanocrystalline silicon has grain orientations along <111>, <220> and <311> planes, with <220> being the most preferable orientation since it produces the least carrier scattering. Schropp described the conditions required for obtaining a perfect <220> oriented

www.manaraa.com

film, based on the filament temperature and silane flowrate [35]. According to his study, the primary condition for obtaining a <220> oriented film is silane depletion and lower flow rates of silane. The depletion of silane prevents the annihilation of atomic hydrogen, the primary cause for the random orientation of the deposited film. The following XRD patterns, corresponding to two different silane flowrates, at various filament temperatures clearly reveal this effect. As shown in the Figure 2.16, at higher silane flow rates, the silane depletes only at higher filament temperatures leading to a prominent <220> peak. But at high temperatures, dissociation of hydrogen to atomic hydrogen is also inevitable that results in <111> peak. But in the case of low silane flow rates, the depletion occurs at much lower filament temperatures, with not much hydrogen dissociation, thus leading to a pure <220> orientation with no <111> peaks.

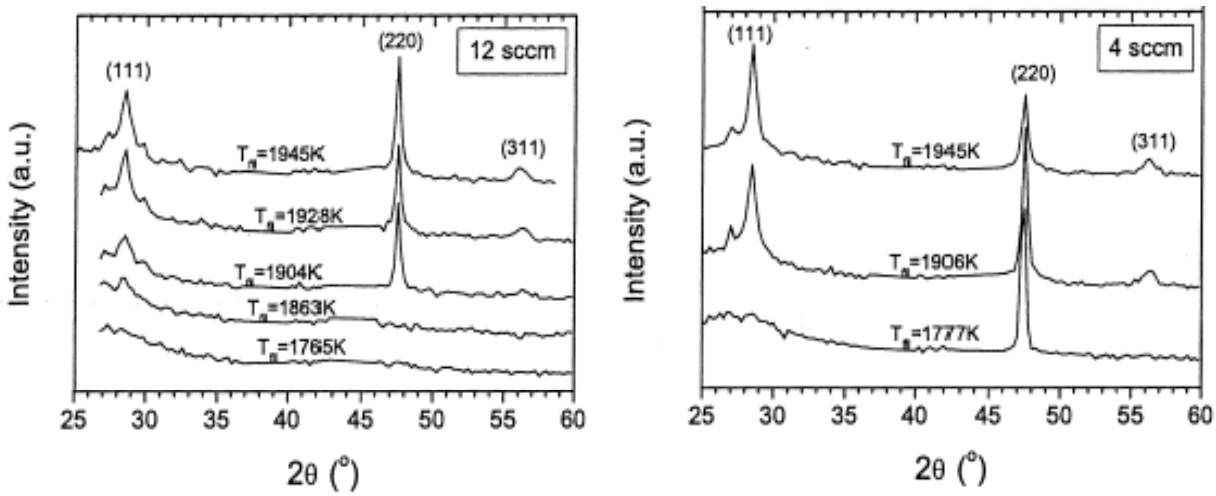

Figure 2.16: XRD patterns for samples deposited at 0.1 mbar and a substrate temperature of 500 °C. The indicated flowrates correspond to silane [28].

Scott Morrison and Arun Madan have reported the variation of <111> and <220> grain sizes with hydrogen dilution at different substrate temperatures. The filament

www.manaraa.com

temperatures they used were 1850-1900 ^{o}C. They concluded that the crystalline grains are predominantly oriented in the <220> direction for films that are in the amorphous to microcrystalline transition region. They stated that the <220> orientation refers to the columnar structure of the grains and is the most preferred orientation for solar cells, since the grain boundaries are parallel to the direction of current flow [36].

Fonrodona et al. had reported <220> grain sizes of 50 nm at a filament temperature of 1500 ^{o}C which decreases significantly at higher temperatures [37]. The effect is reversed for <111> grains, which show a tremendous increase at elevated filament temperatures, reaching upto 70nm as shown in Figure 2.17. The results concluded that a clear transition occurs from <220> to <111> orientation on increasing the filament temperature. This is due to the increased dissociation of hydrogen into atomic hydrogen that causes random orientation of crystalline grains.

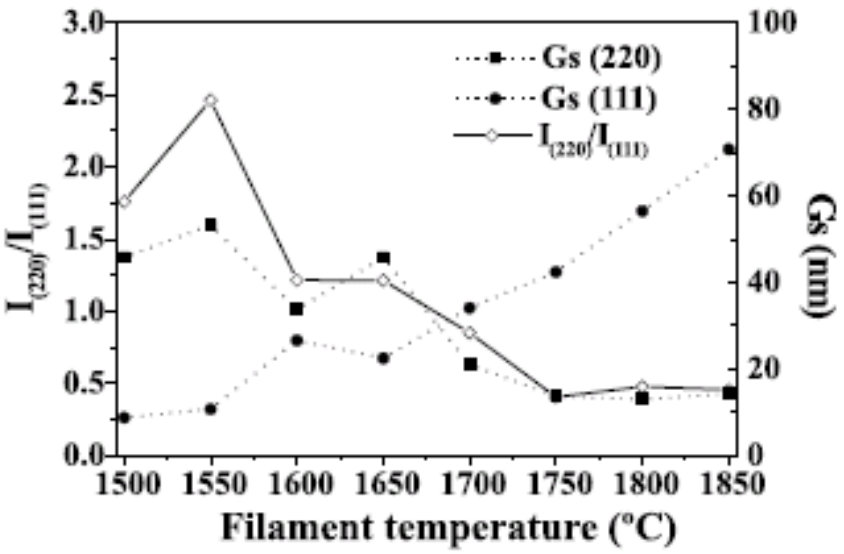

Figure 2.17: Peak intensity ratio and grain sizes along <111> and <220> orientations [37]

www.manaraa.com

In their study, they also observed the concentration profiles of oxygen incorporated into the samples deposited at different filament temperatures. It was concluded that the samples prepared at higher temperatures had a porous structure with high oxygen concentration uniformly distributed throughout the thickness of the film as shown in Figure 2.18.

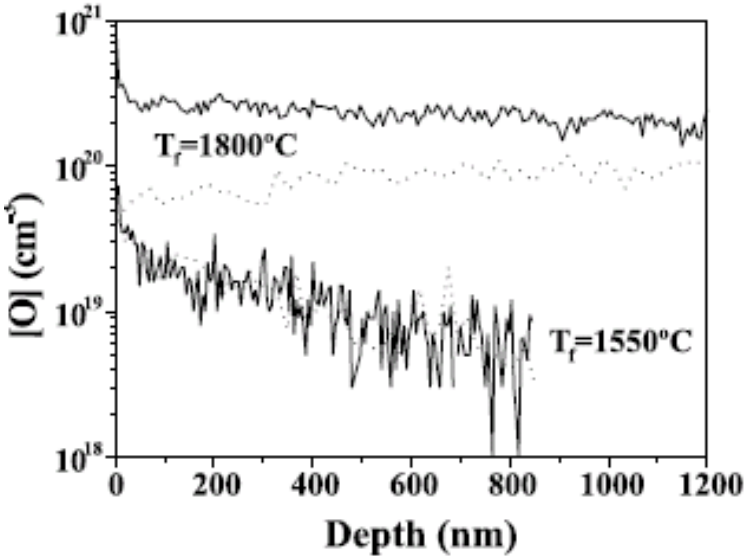

Figure 2.18: Concentration profile of oxygen along the nanocrystalline film thickness measured by SIMS technique [37]

It is also evident from the plot that the oxygen concentration is significantly lower for samples deposited at low filament temperatures, and it decreases along the depth of the film. In this case, the presence of dense amorphous tissues along the grain boundaries, serve as a barrier layer for the diffusion of oxygen into the nanocrystalline film.

2.3 Hot Wire or the Catalytic CVD Process

This technique was first used by Wiesmann in 1979 to deposit hydrogenated amorphous silicon [38]. Matsumura deposited the first polycrystalline films in 1991 using

www.manaraa.com

this technique and also introduced the term CAT-CVD to indicate the catalytic decomposition of gases on the surface of the hot filament used in this technique [39]. Mahan et. al later pioneered this technique in U.S.

The primary reaction in HWCVD is the thermal decomposition of silane into Si and H radicals, on the surface of heated tungsten filament at temperatures greater than 1800 ^{o}C

$$SiH_4 \longrightarrow Si + 4H \quad (2.1)$$

The atomic hydrogen produced in this primary reaction further reacts with silane to give several depositing radicals [40]

$$H + SiH_4 \longrightarrow SiH_3 + H_2 \quad (2.2)$$

$$Si + SiH_4 \longrightarrow 2SiH_2 \quad (2.3)$$

$$Si + SiH_4 \longrightarrow Si_2H_2 + H_2 \quad (2.4)$$

$$Si + SiH_4 \longrightarrow SiH + SiH_3 \quad (2.5)$$

$$Si + SiH_4 \longrightarrow Si_2H_4 \quad (2.6)$$

The SiH_3 will not further react and it becomes the primary precursor for the film growth. The rate constant for the chemical reactions shown above will actually depend on the various deposition parameters such as the pressure, filament temperature and the silane-to-hydrogen ratio. SiH_3 is a very mobile radical with the least sticking co-efficient and can move across a growing surface in search of ideal growth sites, whereas the higher orders of silane such as Si_2H_2, Si_2H_4, Si_2H_6 have a very high sticking co-efficient that makes them less mobile leading to poor quality films.

In PECVD technique, the deposition is influenced by both plasma ions and the radicals. But in case of HWCVD deposition, there no ions present and the entire growth is

www.manaraa.com

governed only by the radicals generated due to thermal decomposition of silane. The composition of radicals generated and their role during actual deposition has been studied by various groups. Kondo et al. explained that the threshold energy needed for SiH_3 radical generation is the minimum when compared to the other radicals as shown in Figure 2.19. Thus according to him, the primary growth precursor in case of both PECVD and HWCVD is the SiH_3 radical. However in HWCVD, the SiH_3 radicals are formed only after the secondary reactions in the gaseous phase.

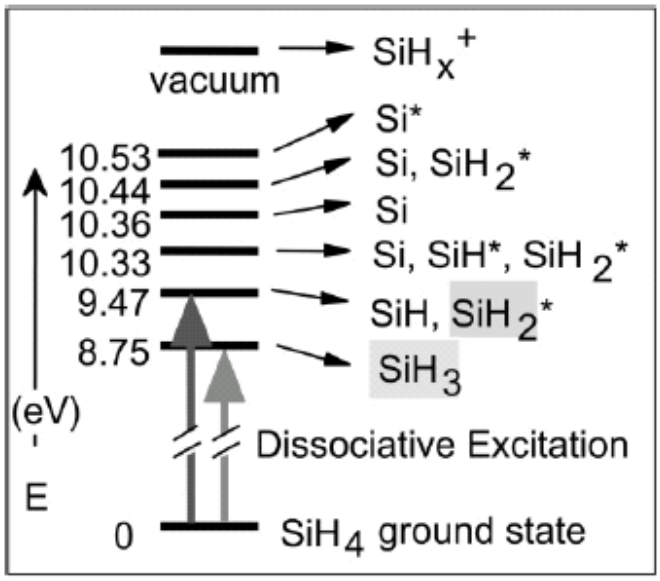

Figure 2.19: Threshold energy for the generation of different radicals [41]

Duan et al. used a new laser based technique called the single photon ionization to probe the radicals generated during hot wire deposition. According to their study, the main radicals present are Si, SiH_3 and Si_2H_6. .They have concluded that Si and SiH_3 arise from the reactions at the surface of the hot filament and not due to gaseous reactions, while the Si_2H_6 radical is generated by the reactions at the chamber wall [42].

www.manaraa.com

In their study Molenbroek et al. have stated that the role of atomic hydrogen is to abstract other H atoms from the growing surface forming dangling bonds which serve as the ideal bonding sites for the mobile silyl radicals [43]. They have concluded that the consumption of all the Si released from the filament surface is critical for obtaining films with good electronic properties.

Nakamura et al. reported that the SiH_3 radicals generated by reaction (2.2), will further undergo gas phase reactions to form Si_2H_6 and silylenes ($HSiSiH_3$). The silylenes are highly reactive and participate in the surface reactions by inserting into Si-H bonds. These unstable radicals also react with SiH_4 to form the stable Si_3H_8 radicals [44].

The surface reactions on the catalytic filament are also very important as it determines the dissociation fraction of the radicals required for deposition. Matsumura et al. clearly illustrated the various reactions on the filament surface occurring at different temperatures [45]. As shown in the Figure 2.20, the silane molecule chemically adsorbs to the tungsten (W) surface, in the form of SiH_3 and H atoms at room temperature. When the temperature of the filament is increased to 600 – 1000 °C, which is in the range of conventional thermal CVD processes, the configuration changes to SiH_2 and 2H atoms. When the temperature is increased further, the SiH_4 radical adsorbs as a single Si atom and four hydrogen atoms. This silicon atom can easily bond with the W atom to form silicides that can decrease the dissociation efficiency of silane by reducing the number of active sites on the catalytic filament. The adsorbed Si and H atoms can be desorbed from the surface by increasing the temperature beyond 1600 °C.

www.manaraa.com

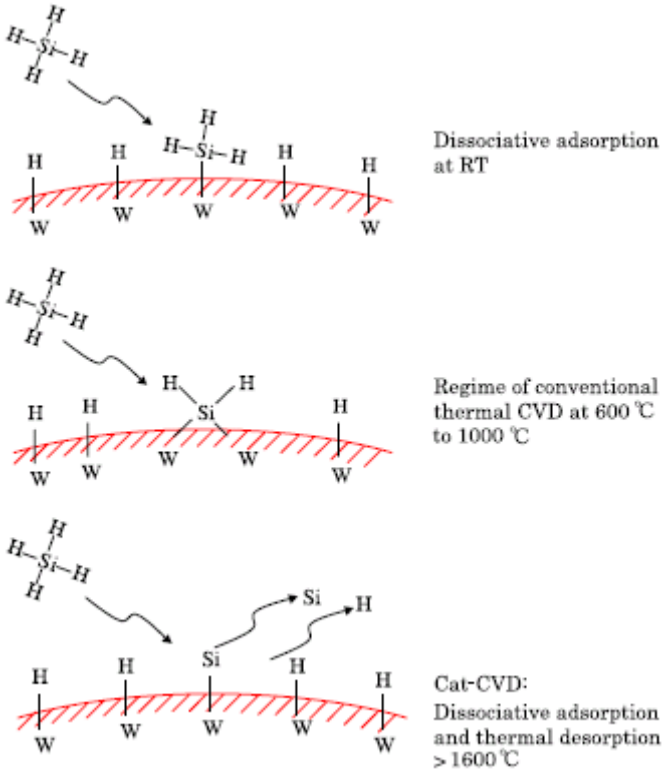

Figure 2.20: Schematic of the different reactions on the filament surface at various temperatures [45]

2.4 Solar Cells with Nanocrystalline Intrinsic Layers Fabricated by HWCVD

Nanocrystalline solar cells need a much thicker absorber layer due to the inherent low absorption co-efficient of the base layer. This demands higher deposition rates which brings along many complications with it. The critical factors involved in increasing the deposition rate are the filament temperature, the pressure and the silane concentration. If the filament temperature is made too high, the radiant heating from the filament significantly affects the substrate temperature which modifies the film properties. When the chamber pressure is increased beyond a certain threshold vale, then secondary reactions can occur between the gas species due to increased number of collisions leading to the formation of undesirable

www.manaraa.com

radicals. The other main parameter which influences the film properties to a much greater extent is the silane concentration. If a very high concentration is used, then it leads to the formation of crystalline film of porous nature and higher concentrations leading to the formation of amorphous material with increased defect densities [46]. Thus the recent trend is to fabricate the nanocrystalline solar cells in a region close to the transition to amorphous phase, which contain crystalline grains with non-porous grain boundaries made of compact amorphous tissues. Klein et al. reported nanocrystalline silicon solar cells with record efficiency of 9.4% and a open circuit voltage of 600mV fabricated using HWCVD at a low deposition rate of 1Å/s [46]. Thus the challenge is to get a good quality nanocrystalline device combined with high deposition rates.

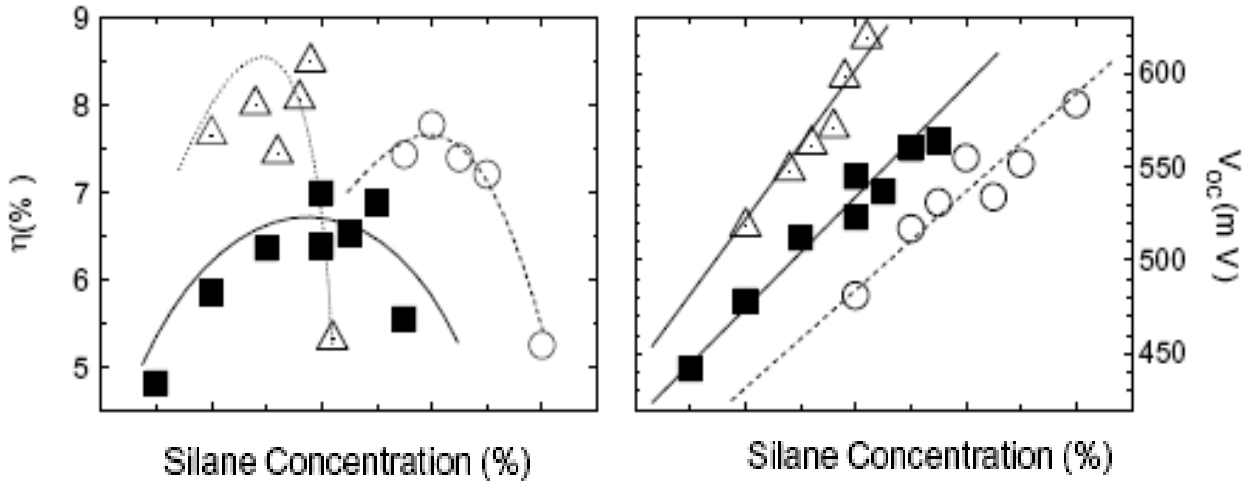

Figure 2.21: Influence of silane concentration and substrate temperature (Ts) on the efficiency and open circuit voltage of the nanocrystalline device. Open triangle: Ts=185 °C, Open circle: Ts=210 °C, Closed square: Ts=220 °C [46]

The effect of silane concentration and the substrate temperature on the electrical characteristics of the device is clearly shown in Figure 2.21. As shown in the plots, the

www.manaraa.com

efficiency reaches a maximum value only at a moderate value of silane concentration. The low and high open circuit voltages (Voc) corresponding to the two extremes of silane concentration are clear indications of crystalline and amorphous materials respectively. It is also evident from the plot that maximum efficiency can only be attained at low substrate temperatures.

As mentioned earlier, nanocrystalline silicon solar cells demand a much thicker intrinsic layer. But when the thickness is increased beyond a certain level, the Voc drops significantly and this affects the fill factor of the device to a great extent. In their study, Klein et al. have reported solar cells with a maximum efficiency of ~ 9.4% combined with good electronic properties at a optimum intrinsic layer thickness of ~1.3 µm.

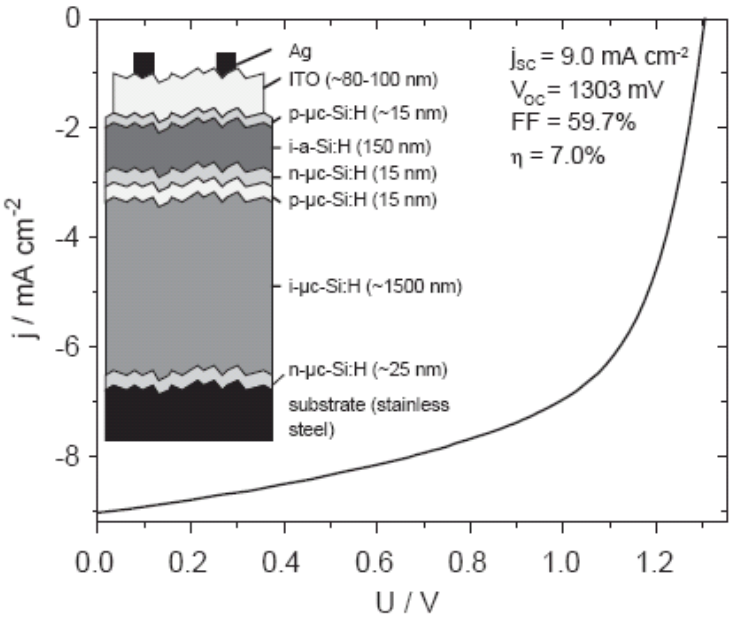

Figure 2.22: Structure and I-V characteristics of a micromorph nipnip tandem solar cell [47]

Kupich et al. have integrated the amorphous and microcrystalline absorber layers to form a unique type of tandem solar cells called the “micromorph” solar cells [47]. The best

www.manaraa.com

efficiency attained in these devices is 7% for nipnip configuration with a Voc of 1303 mV and a fill factor of 59.7% as shown in Figure 2.22. The other important feature in this device is that, all the layers were deposited only by HWCVD.

Strengers et al. explored the effect of the intrinsic layer thickness on the electrical characteristics of the solar cell fabricated by hot wire CVD [48]. According to their experimental results and simulations, the open circuit voltage V_{OC}, and the short circuit current J_{SC}, increase sharply when the thickness of the absorber layer was increased from 500nm to 1000nm. But no significant change was observed after 2000nm as shown in the following plot.

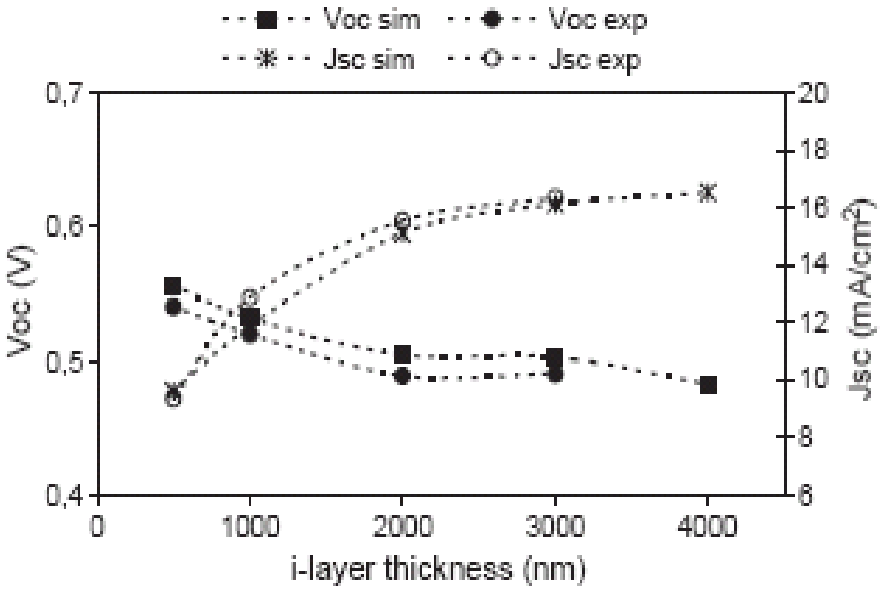

Figure 2.23: Effect of the intrinsic layer thickness on the device I-V characteristics [48]

H. Li et al. showed the improvement of V_{OC} and fill factor for solar cells with microcrystalline intrinsic layers when compared to the devices with polycrystalline layers [49]. As shown in Figure 2.24, the improvement in V_{OC} was more than 10%, but the J_{SC} decreased for microcrystalline devices. Based on their XRD results, Li et. al., concluded that

www.manaraa.com

the reduced <220> orientation in the microcrystalline material reduces the light trapping efficiency of the absorber layer, which ultimately decreases J_{SC}.

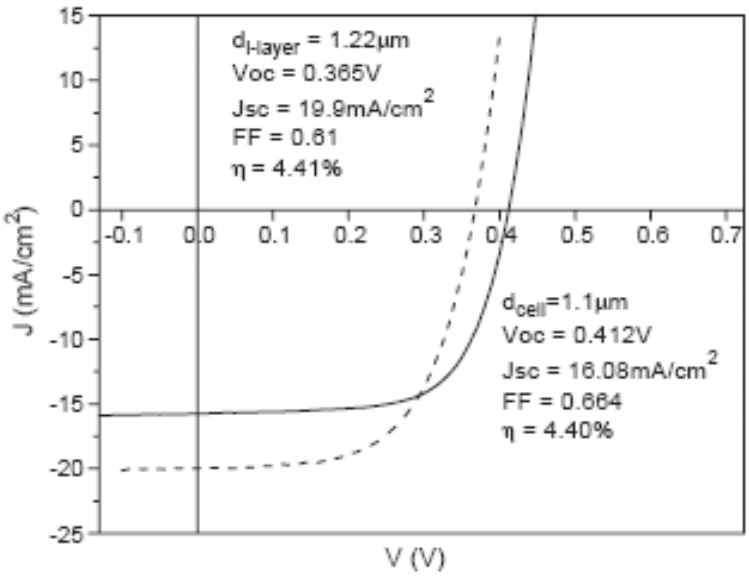

Figure 2.24: Comparison of I-V characteristics of solar cells with (a) microcrystalline intrinsic layer (solid line) (b) polycrystalline intrinsic layer (dotted line) [49]

www.manaraa.com

CHAPTER 3: EXPERIMENTAL SET-UPS

3.1. Device Fabrication

3.1.1. Combined Hot Wire ECR PECVD Reactor

All the films and intrinsic layers for the solar cells were deposited using the reactor shown in Figure 3.1, which had the ability to combine both hot wire and ECR PECVD techniques. Hot wire depositions were carried out using tantalum filaments which were 0.5 mm in diameter and about 40 cms in total length. One of the unique features in this reactor is the distance between the filaments and the sample which is about 11cm and its been verified experimentally that this arrangement prevents the sample heating due to radiation from the filaments.

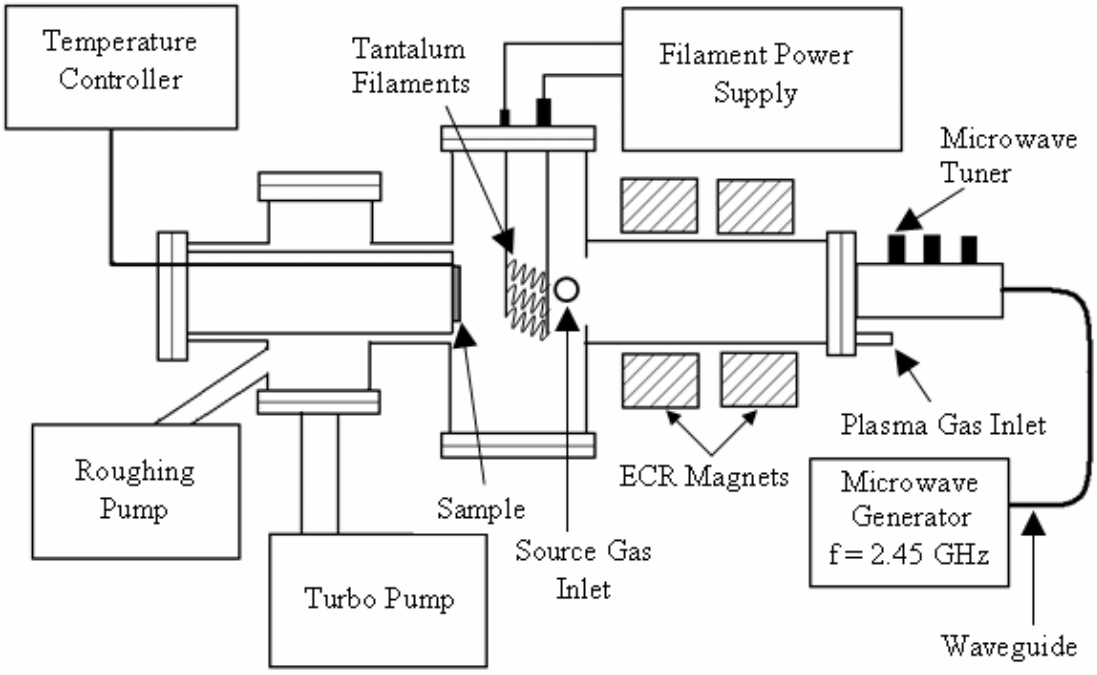

Figure 3.1: Schematic of the combined Hot wire – ECR PECVD reactor

www.manaraa.com

Most of the other groups, work with a very low filament-substrate distance, a typical value being 3- 4 cm. This can be a major drawback with the reactor design, since at such low distances, the radiation from the filament will definitely increase the substrate temperature significantly. Klein et al. work with a filament-substrate distance of 7 cm and in one of their work, they have reported that their substrates are heated to 185 ^{o}C solely by the radiation from two filaments [31].

The surface temperature measurement was performed using a dummy stainless steel substrate of considerable thickness and a fine hole drilled along its side. A thermocouple was inserted through this orifice and carefully held in position. The following plot shows the influence of filament temperature on the substrate.

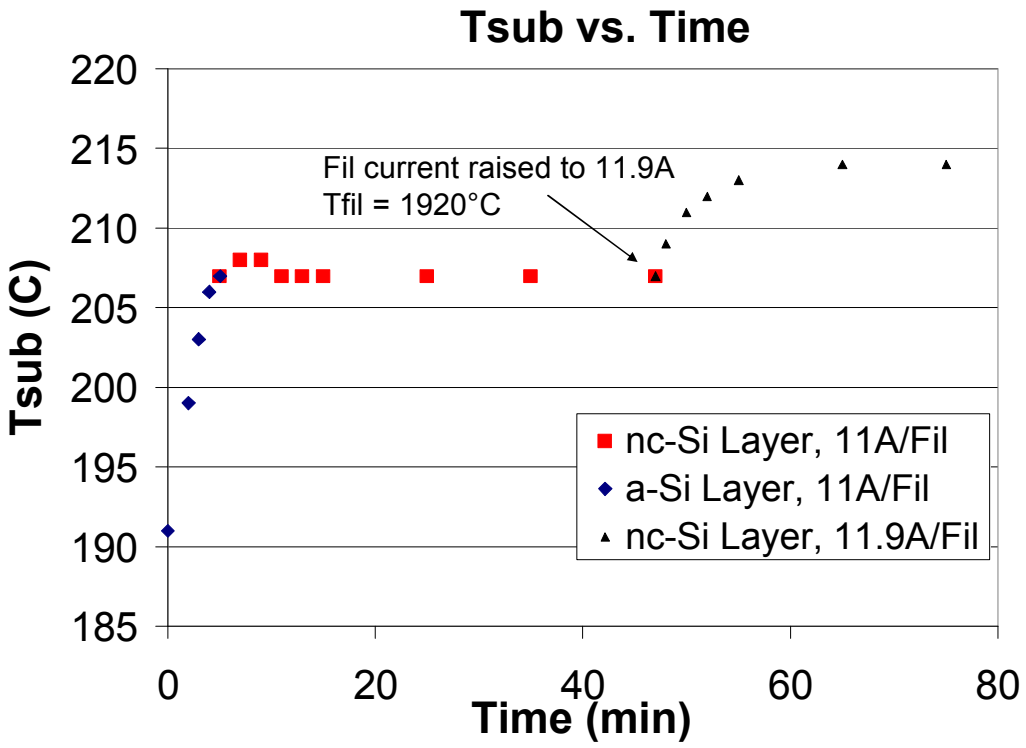

Figure 3.2: Filament temperature effect on substrate temperature

www.manaraa.com

Here we have measured the substrate temperature during an actual deposition on our dummy substrate. The set point for the substrate temperature was 200 ^{o}C. As shown in the plot, at a filament current of 11 A corresponding to a temperature of 1860 ^{o}C, the increase in the substrate temperature was only 7 ^{o}C. At a maximum filament current of 11.9 A corresponding to a temperature of 1920 ^{o}C, the increase in substrate temperature was only 14 ^{o}C which is the minimum, when compared to that of the other groups.

The substrate temperature was controlled at 250 ºC and most of the depositions were done at a pressure of 10mT. A staggered filament design as shown in Figure 3.3 was used in the current setup to account for the filament sagging due to thermal expansion. The filaments were replaced every two runs and after the first run the filaments were cleaned by flowing hydrogen through the chamber at 25mT at a filament current of 11A in order to burn the silicides formed over the surface.

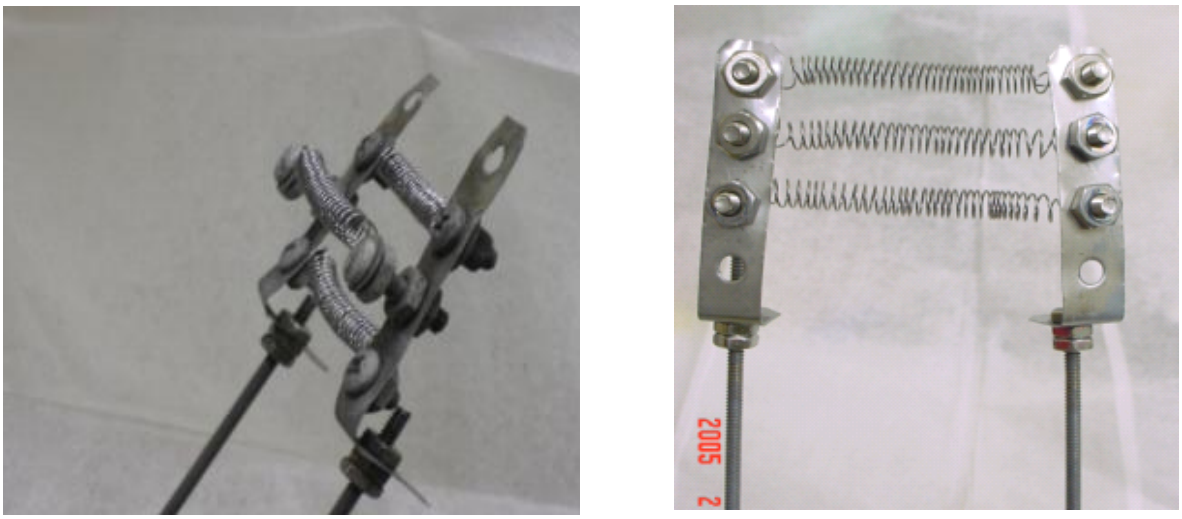

Figure 3.3: Staggered design of the hot wire tantalum filaments

www.manaraa.com

The filaments were held by two stainless steel rods mounted parallel to the substrate and isolated from the ECR chamber where the plasma was generated. The pressure in the chamber was established using a turbomolecular pump which is backed up up a separate mechanical pump and a backing pump. The substrate was heated by a Watlow PID controller connected through a thermocouple and fixed to the outer side of the substrate holder through a recessed grove which is well insulated from the ambient air. Separate feedthroughs are provided in the reactor to separate the plasma gases such as hydrogen and helium from the main deposition gas which is silane in our case.

3.1.2. ECR Deposition

The ECR system consists of a 2.45 GHz microwave generator, three stub tuner and two temporary magnets independently controlled by separate power supplies. The microwave from the source is directed to the tuner by the waveguide and then introduced into the chamber through the quartz window which acts as a coupler and also as a vacuum sela between the tuner and the process chamber. A restricting orifice separates the ECR chamber from the hot wire chamber and also helps in diverging the plasma to the central chamber where the sample is mounted. The magnets are controlled by two DC power supplies and by tuning the current supplied, the plasma density can be varied. The magnets are positioned in such a way that the magnetic flux density near the source (rear) magnet is approximately 875 Gauss, which is the required condition for resonance to occur between the incoming microwave and the frequency of rotation of electrons in the plasma [50]. During the combined hot wire and ECR runs the following procedure was followed before opening the shutter to the substrate (i) the plasma was turned on and stabilized by tuning the current

www.manaraa.com

supplied to the magnets (ii) the hot wire filaments were turned on to the required filament temperature (iii) the hot wire filaments were turned off quickly to see if the plasma was still stable with no flickering and with low reflected power (iv) the hot wire filaments were turned on finally for the entire run.

3.2. Design of the Solar Cell

The solar cells fabricated were p+nn+ configuration with 'n' as the base layer. Polished stainless steel was used as the substrate and a transparent ITO sputtered onto the p+ layer served as the final contact. The n+ and p+ layers were deposited in a VHF PECVD reactor at 45 MHZ while the intrinsic layer was deposited in the HWCVD reactor with 3 parallel filaments configuration. The p+ is deposited as a thin nanocrystalline layer forming the interface with intrinsic layer, followed by a very thin amorphous layer which prevents the oxidation of the top surface.

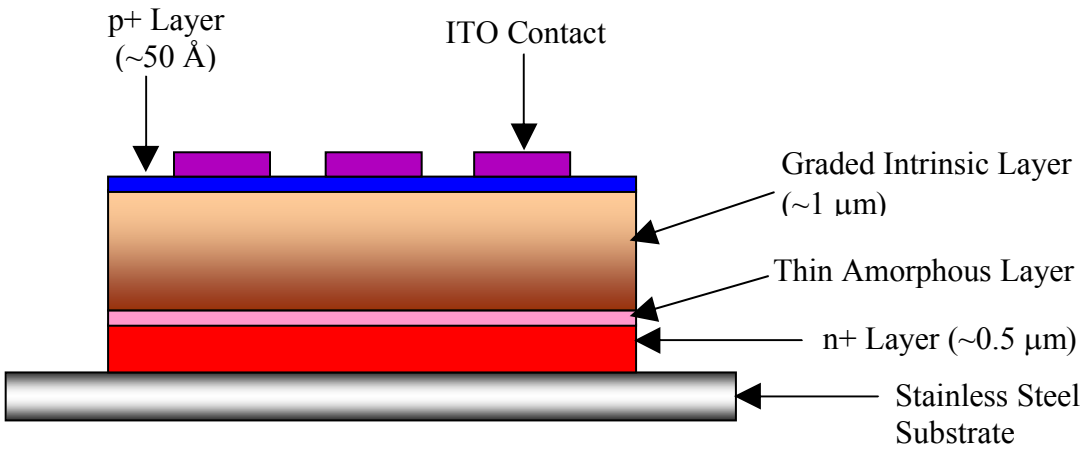

Figure 3.4: Cross-section of a working solar cell

www.manaraa.com

The intrinsic layer deposition was started with a high hydrogen dilution ratio which was ~5:1 for most of the devices and graded for every 5 minutes to a final ratio as low as 1.4:1. To compensate for the oxygen that is unintentionally doped into the base layer, ppm levels of boron was introduced during the deposition. In order to create a smooth steep electric profile for efficient carrier collection, the boron doping was graded every 2 minutes along with the regular deposition for about two-thirds of the i-layer thickness. The resulting band diagram is shown in Figure 3.5 .

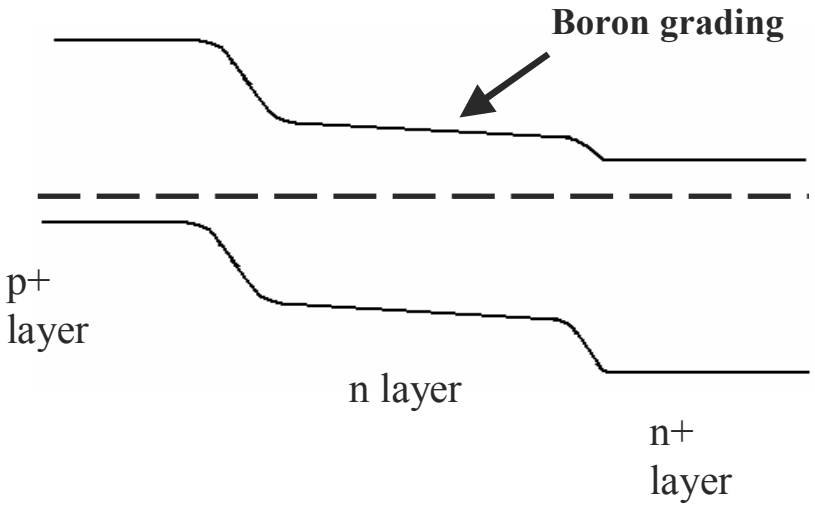

Figure 3.5: Band diagram for the nc-Si:H solar cell

In a working device with the intrinsic layer being slightly n-type, the collection of holes is very important, since they essentially are the minority carriers except near p+-n interface region. As shown in the band diagram, by this grading profile, the holes generated near the n+-i interface were collected more efficiently due to the inbuilt electric field.

www.manaraa.com

3.3 Thin Film Characterization Techniques

3.3.1. Thickness Measurement

The thickness of the devices was measured using a UV/NIS/NIR spectrophotometer. In this dual beam apparatus, one of the monochromatic beams travels unobstructed, while the second beam is made to incident on the sample using a mirror assembly creating an interference pattern due to the reflection from the top and bottom surfaces of the sample. Both the monochromatic beams are finally collected by a photo detector which evaluates the difference in their intensities.

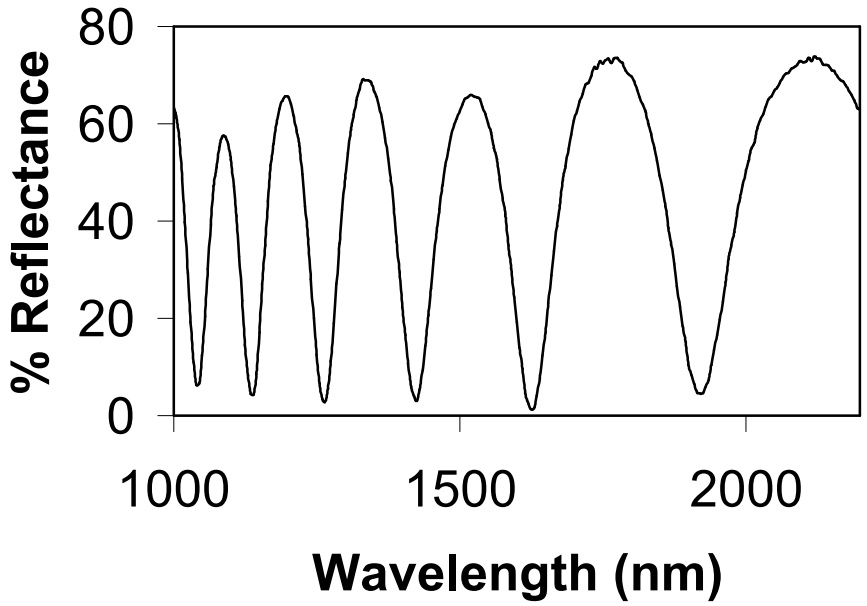

Figure 3.6: Reflection spectra used for thickness calculation

Figure 3.6 shows a reflection spectrum for one of the devices which clearly indicates the formation of peaks and valleys created due to interference. The thickness is evaluated as shown in Equation 3.1

www.manaraa.com

$$t = \frac{\lambda_1 * \lambda_2}{2 * (n_1\lambda_2 - n_2\lambda_1)} \tag{3.1}$$

where λ_1 and λ_2 are the wavelengths corresponding to the adjacent peaks or valleys and n_1 and n_2 are the corresponding refractive indices.

3.3.2. Raman Spectroscopy

When light is incident on a sample, the incident photons are absorbed by the material and they are scattered. A majority of the photons are scattered elastically where there is no difference in wavelength between the incident and the scattered photons and this phenomenon is called Raleigh scattering. The second type which is called as the inelastic scattering also known as the Raman scattering has a significant shift in wavelength between the incident and scattered photons. In in-elastic scattering, photons either create phonons referred as stokes or they annihilate the phonons also known as anti-stokes. These phonons vibrate in the lattice with a certain frequency which is a characteristic of each individual material and accordingly a sharp peak is obtained in the final spectra at a wavelength corresponding to the vibrating frequencies of the phonons.

In Raman spectroscopy we analyze the shift in wavelength of the emitted photons also known as the Raman shift. The instrument used for the analysis was a inVia Reflex Raman Microscope by Renishaw, where in a laser beam is incident on the samples and the scattered photons being collected by a CCD. The shift in wavelength or the wavenumber (cm^{-1}) is finally plotted against the intensity of the scattered radiation. A typical Raman plot for a nanocrystalline silicon film is shown in Figure 3.8.

www.manaraa.com

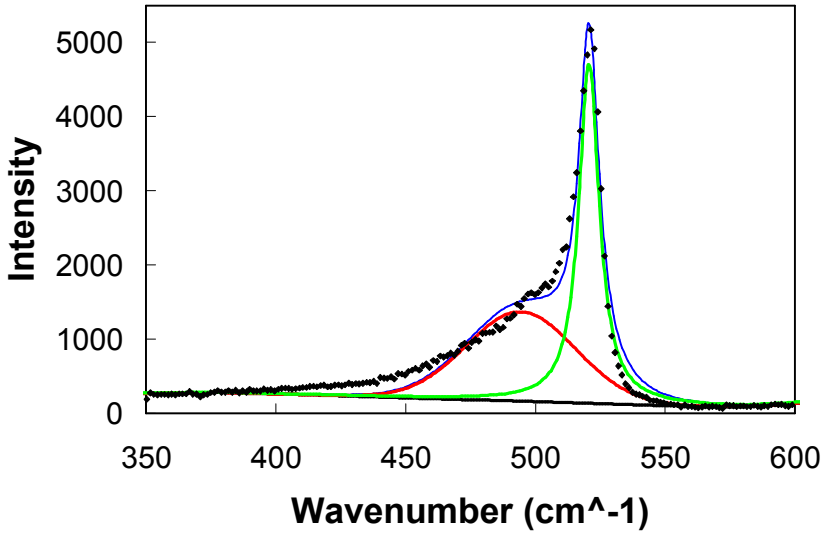

Figure 3.8: Raman plot for a nanocrystalline silicon film

The above plot shows the raw data which has been fit to two different peaks at ~480 cm-1 using a Gaussian fit representing the amorphous phase and at ~520 cm-1 using a Lorenztian fit representing the crystalline phase [51]. As seen from the plot the maximum intensity of the crystalline phase is 4593 and for amorphous phase it is 1206. The ratio of these two peaks is usually considered to be a signature of the degree of crystallinity of the film. Thus the final crystalline ratio of the film is evaluated to be 3.8.

3.3.3. X-Ray Diffraction

XRD measurements are based on Bragg's law which is given by the following equation,

$$n\lambda = 2d\sin\theta \tag{3.2}$$

where 'λ' represents the wavelength of the incident X-ray beam, 'd' refers to the distance between the lattice planes of the sample and 'θ' is the angle of incidence for the X-ray beam.

www.manaraa.com

Thus according to Bragg's law when the wavelength of the incident X-ray beam is equal to the distance between the periodic lattice planes in a crystalline material, then the photons are reflected. These photons are collected by a detector and they form the crystalline peaks in diffraction spectra. A Siemens X-Ray diffractometer with a sealed copper anode X-Ray used was used for the measurements. A typical XRD plot for a nanocrystalline film is shown in Fig. 3.9 wherein '2θ' is plotted against the intensity of the reflected beam which is the photon count.

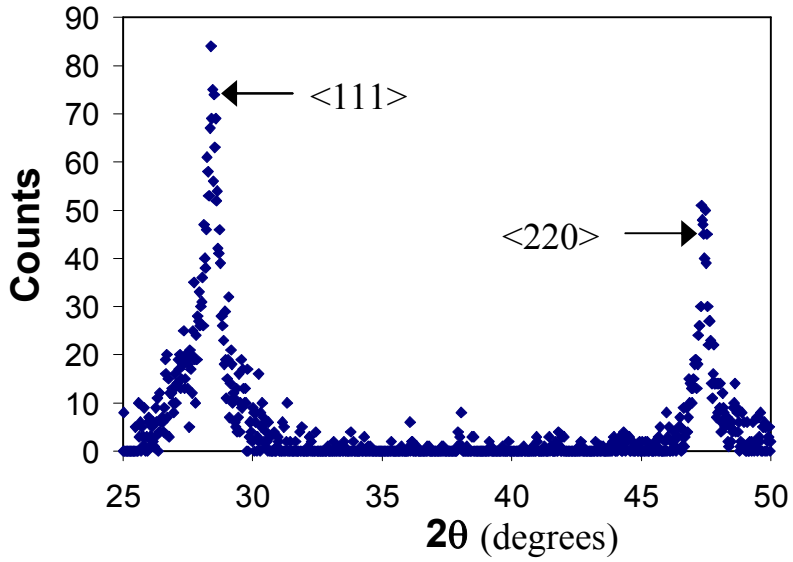

Figure 3.9: XRD plot for a nanocrystalline film

As shown in the plot, two distinct peaks appear in the diffraction spectra for nanocrystalline films. The peak at ~28.5 degrees represents the <111> orientation of the crystalline grains, and the peak at ~47 degrees corresponds to the <220> orientation. The other important parameter derived from the XRD measurement is the size of the crystalline grains. The grain size is evaluated using Scherer's formula [52] as shown in Equation 3.3.

www.manaraa.com

$$d = \frac{0.9\lambda}{\beta \cos\theta} \tag{3.3}$$

wherein 'd' is the grain size, 'λ' is the wavelength of the X-rays, 'θ' is the angle of incidence for the X-ray beam and 'β' is the Full Width Half Maximum (FWHM) of the individual crystalline peaks.

3.4. Device Characterization Techniques

3.4.1. I-V Characterization

The I-V characteristics gives us much valuable information on the efficiency of the solar cell, short circuit current density due to carrier generation under illumination with no bias and the open circuit voltage of the device which is dependant upon the bandgap of the material. The equivalent circuit of the solar cell is as shown in Figure 3.10. The current voltage relationship for the device is given by the following equation,

$$I = -I_{ph} + I_0\left[\exp\left(\frac{qV}{nkT}\right) - 1\right] \tag{3.4}$$

where I_0 is the reverse saturation current, V is the bias or voltage applied, n is the diode factor and I_{ph} is the photocurrent. The short circuit current which corresponds to a load resistance of zero and V=0, depends to a large extent on the absorption efficiency of the intrinsic layer used in the device and in a good device, the design will be optimized to match the absorption

www.manaraa.com

spectra of the intrinsic layer with the solar spectra so that maximum number of incident photons are captured.

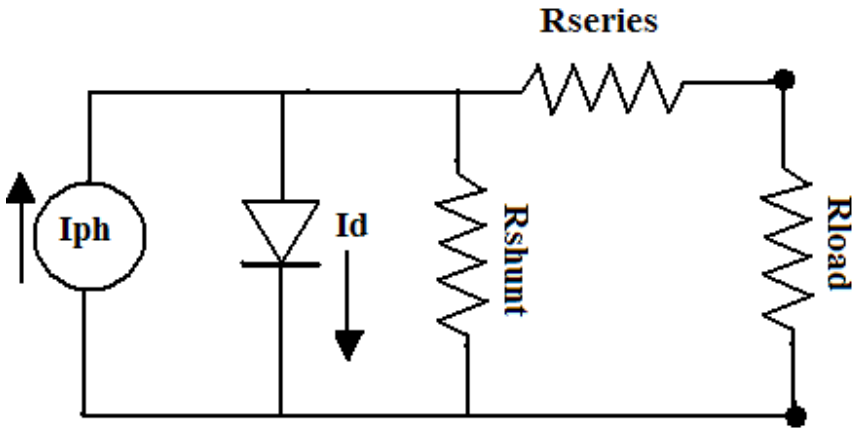

Figure 3.10: Equivalent circuit of a solar cell

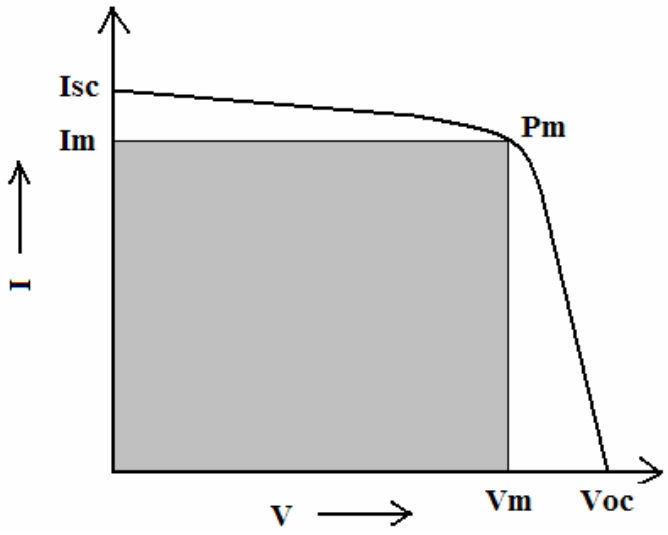

Figure 3.11: Typical I-V curve for a solar cell device

From Equation 3.4, it can be seen that the short circuit current equals the photocurrent, Isc = I_{ph} at V=0. A typical I-V curve for a device is shown in Figure 3.11. The

www.manaraa.com

second parameter is the open circuit voltage (V_{oc}) which corresponds to the condition when I=0. Thus from the I-V equation, the expression for V_{oc} can be given by,

$$V_{oc} = \frac{nkT}{q} \ln\left[\frac{I_{ph}}{I_o} + 1\right] \tag{3.5}$$

The reverse saturation current I_0 is strongly dependant on the bandgap of the material which also makes the V_{oc} material dependant. Typical values of V_{oc} for a-Si solar cells are 0.8–0.9 V, and 0.4–0.5 V for nc-Si devices. The next important parameter in the device characteristics is the fill factor represented by the shaded area in Figure 3.11. The fill factor is evaluated by the following equation,

$$Fill\ \ Factor = \frac{V_m \times I_m}{V_{OC} \times I_{SC}} \tag{3.6}$$

Thus if the series resistance of the solar cell is very low and the shunt resistance is very high, then the I-V curve will be close to a square shape which will yield high fill factors. This can be achieved in devices that have very good electrical contacts, strong inbuilt electric field in the intrinsic layer and very low defects at the interfaces of absorption layer which would otherwise trap the generated carriers. High efficiency nc-Si solar cells have fill factors in the range of 65-70%. The final factor is the efficiency of the solar cell η, represented as the ratio of incident power to the output power, given by the following equation,

$$\eta = \frac{FillFactor \times V_{OC} \times I_{SC}}{P_{IN}} \tag{3.7}$$

www.manaraa.com

3.4.2. Quantum Efficiency Measurement

The quantum efficiency of the devices is measured using the set up shown in Figure 3.12. The samples are soaked in a fixed DC light so as to fill all the midgap states with photogenerated carriers. A separate beam of light from the monochromator is chopped at a frequency of 13.5 Hz and this serves as the AC signal for photogeneration. The lower frequency helps preventing noise from the regular 60 Hz current used in these equipments. The wavelength is scanned from 400nm to 900nm and in order to prevent the lower wavelength beams from interfering with the measurements at much higher wavelengths, a 700nm filter is used. The AC beam from the filter is focused on to the sample using a mirror and is superimposed with the DC beam thus varying the photocurrent produced in the sample due to carrier generation. This signal is pre-amplified and sent to a lock in amplifier to track the variation of photocurrent with wavelength. For nanocrystalline devices, the Q.E measurements are done under zero and a small reverse bias voltage of -0.5V.

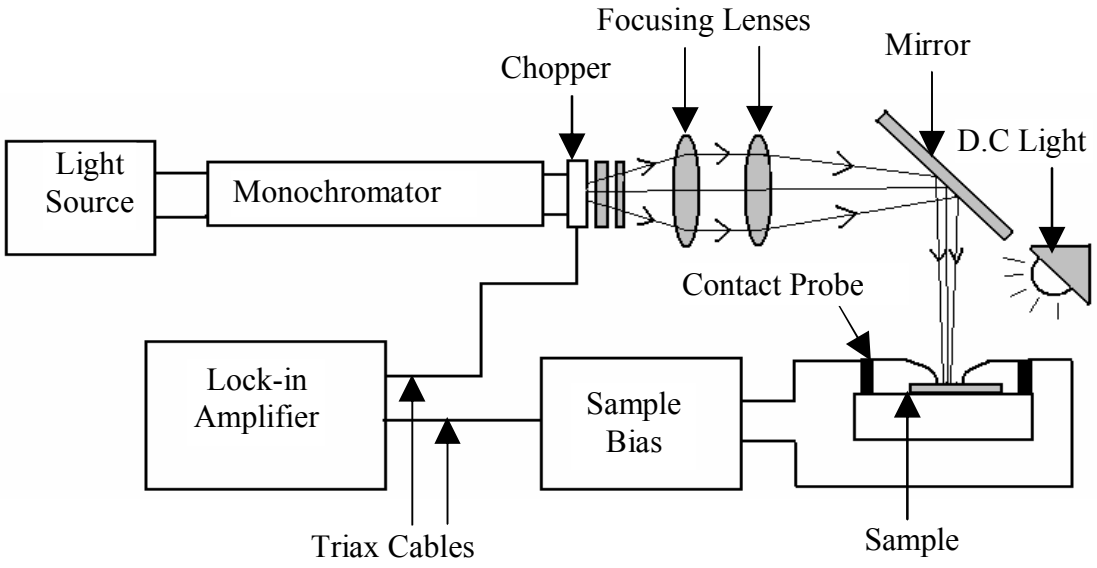

Figure 3.12: Schematic of the quantum efficiency set-up

www.manaraa.com

The measurements done under bias gives us more information about the electric field profile in the device and by comparing the results with no bias condition, problems in the device design can be cleverly interpreted. Figure 3.13 shows the Q.E plots for a good working device with high efficiency.

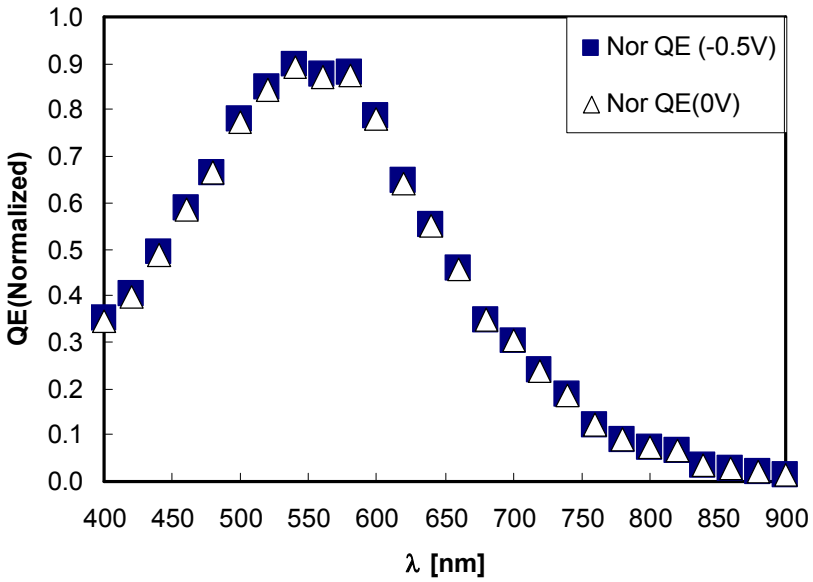

Figure 3.13: Sample Q.E plot of a working nc-Si:H solar cell

The Q.E spectra at shorter wavelengths correspond to the high energy photons which mostly get absorbed in the first few layers of the device. Thus they give us valuable information about the collection of minority carriers near the p+-n interface which are the electrons. The Q.E at longer wavelengths correspond to the region near the n+-n interface and higher Q.E ratios between bias and zero bias conditions in this regime, would indicate that there is some device problem in collecting the minority carriers (holes) generated near the n+-i interface. For a nanocrystalline device we increase the electric field under reverse bias to observe if it enhances the carrier collection and for a good device as shown in

www.manaraa.com

Figure 3.13, there should be no difference in the two spectrums since there is already a good carrier collection established under zero bias.

3.4.3. Capacitance-Voltage (CV) Measurements

The doping density or the shallow defect density and the deep defect density in the devices fabricated were evaluated from the CV data based on Kimerlings model [53]. The model predicted that under reverse bias and at lower frequencies, the capacitance voltage curve shows two distinct regions as shown in Figure 3.14. In the first region where the capacitance increases sharply with the reverse bias, the slope corresponds to the donor density or the shallow state defect density whereas the slope of the second region is used to evaluate the deep defect density. The low frequency is necessary to give enough time for the deep state carriers to respond to the applied bias. Also, only at higher reverse bias, the deep level defects start to respond to the measurement. The difference between the two values gives the actual defect density in the sample.

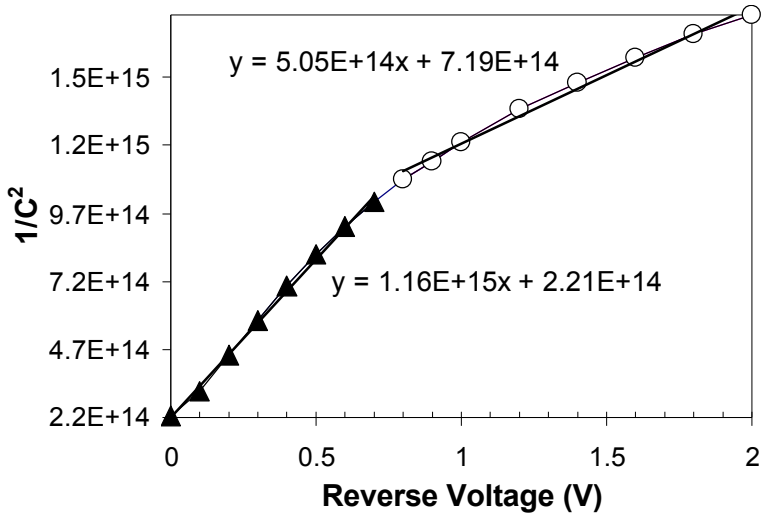

Figure 3.14: Typical C-V plot for a nc-Si solar cell

www.manaraa.com

Thus based on the slopes in the plot shown in Figure 3.14, the donor density is evaluated to be 1.08 x10^{16} cm^{-3} and the deep defect density is 1.74 x10^{16} cm^{-3}. The measurements are done at a frequency of 120 Hz and a drive voltage of 100mV. The entire setup is covered to prevent the light from interfering with the measurements.

3.4.4. Diffusion Length of Minority Carriers

The diffusion length was evaluated by combined C-V and quantum efficiency technique as described by Dalal et. al [54, 55]. The following theory will explain the assumptions and derivation involved in the diffusion length.

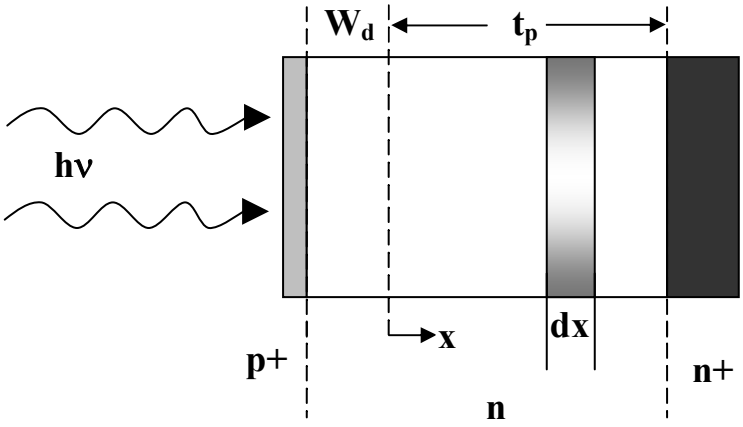

Figure 3.15: Schematic of a illuminated p+nn+ solar cell

In our devices, holes are considered to be the minority carriers since the base layer is slightly n-type. Consider a p+nn+ nanocrystalline solar cell with the light shining from the p+ side, as shown in Figure 3.15. Light is incident from the p+ layer of the cell which has a negligible thickness of t_1. The width of the depletion layer formed in the n type base layer is W_d and the thickness of the undepleted base layer is 't_p'. We know that the quantum efficiency is

www.manaraa.com

proportional to the number of absorbed photons. Thus the light absorbed in different layers is given by the following equations,

Considering the p+ layer alone,

$$\#\ of\ \ absorbed\ \ photons \quad \propto \quad 1-e^{-\alpha t_1}=0 \quad (for\ t_1 << 1) \tag{3.8}$$

Considering p+ layer along with the depletion layer formed in the n type base layer,

$$\#\ of\ \ absorbed\ \ \ photons \quad \propto \quad e^{-\alpha t_1}(1-e^{-\alpha W_d}) \tag{3.9}$$

Now let us consider a small portion in the base layer which is far away from the p+-n interface shown as the shaded region in the schematic. The quantum efficiency of the undepleted base layer can be derived by integrating the absorbed photons in the shaded region over the entire thickness t_P as given by the following expression,

$$Q.E = \int_0^{t_P} e^{-\alpha(t_1+W_d)} e^{-\alpha x} \alpha e^{-x/L_P} dx \tag{3.10}$$

$$= e^{-\alpha W_d} \alpha \int_0^{t_P} e^{-x/L_P(1+\alpha L_P)} dx \tag{3.11}$$

$$= e^{-\alpha W_d} \cdot \left(\frac{\alpha L_P}{1+\alpha L_P}\right)\left[1-e^{-t_p/L_p(1+\alpha L_P)}\right] \tag{3.12}$$

Thus the quantum efficiency of the entire solar cell can be estimated by adding the absorption in each of the layers as shown in the following Equations (3.13) & (3.14).

www.manaraa.com

$$Q.E = 1 - e^{-\alpha W_d} + e^{-\alpha W_d} \cdot \left(\frac{\alpha L_P}{1 + \alpha L_P} \right) \left[1 - e^{-t_p / L_p (1+\alpha L_P)} \right] \tag{3.13}$$

$$= \alpha W_d + \left(\frac{\alpha L_P}{1 + \alpha L_P} \right) \left[1 - e^{-t_p / L_p (1+\alpha L_P)} \right] \tag{3.14}$$

For very low α and the thickness of the absorber layer being greater than the diffusion length of the minority carriers, the above expression can be simplified to,

$$Q.E = \alpha W_d + \left(\frac{\alpha L_P}{1 + \alpha L_P} \right) \tag{3.15}$$

$$\Rightarrow Q.E \cong \alpha (W_d + L_P) \tag{3.16}$$

The depletion width in the above equation is evaluated from C-V measurements under reverse bias and the values are plotted against quantum efficiencies evaluated at 950nm based on the dual beam technique explained previously. Very high wavelength is chosen because the incident photons have to travel a long distance into the base layer before they are absorbed and the generated holes have to diffuse to the edge of the depletion layer in order to get collected by the p^+ layer. A typical plot for the diffusion length measurement is shown in Figure 3.16. The diffusion lengths evaluated from the intercepts on depletion width axis are 0.07 µm and 1.7 µm for samples of crystalline ratios 3.5 and 2 respectively. As shown in Figure 3.17, the theoretical Q.E is also calculated based on the diffusion length and compared with the experimental values. Good agreement between the two values validates the assumptions made in this measurement.

www.manaraa.com

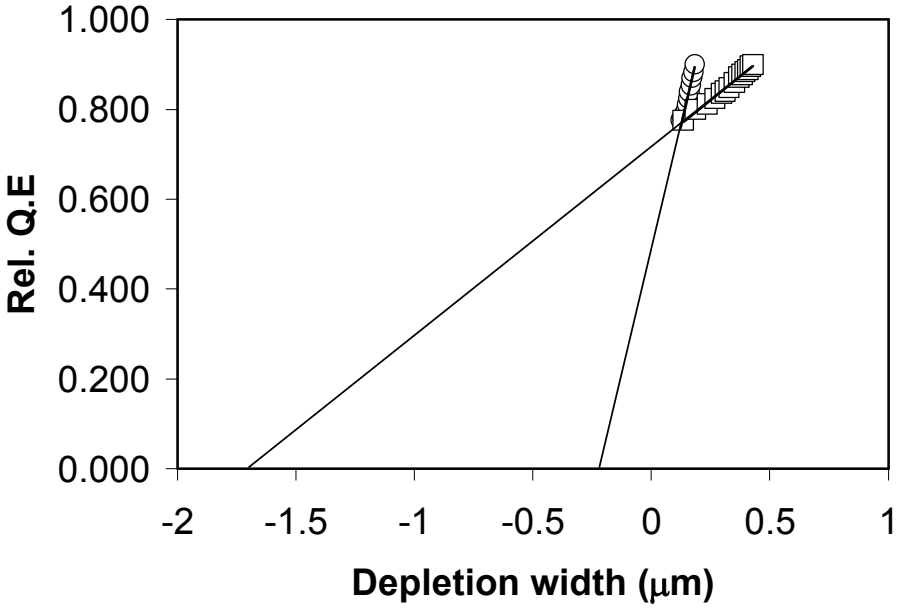

Figure 3.16: Calculation of Diffusion length from the intercept of Q.E vs W_D

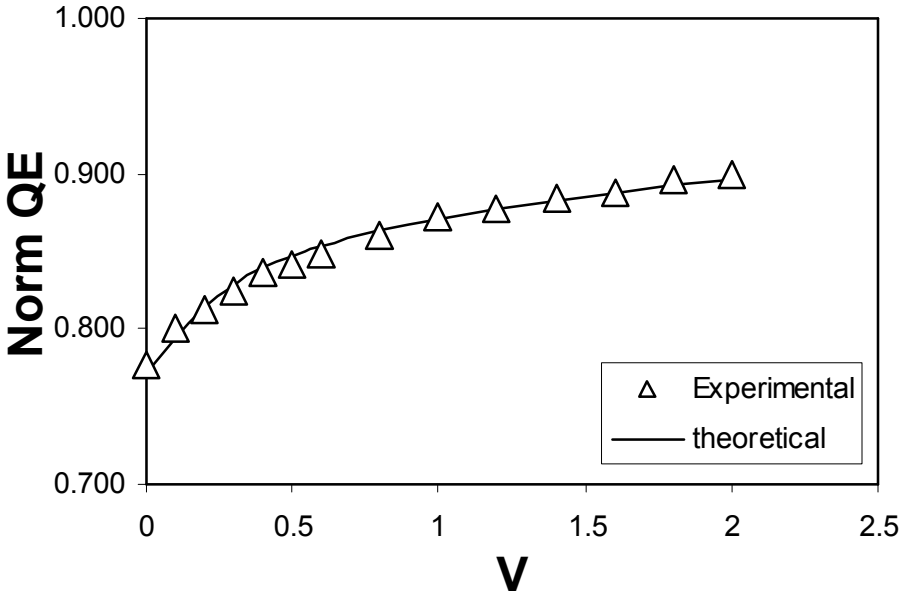

Figure 3.17: Comparison of theoretical and experimental values

www.manaraa.com

3.4.5. Device Contacts

The contacts for the p-i-n devices are formed by depositing thin transparent dots of Indium Tin Oxide (ITO) using a reactive sputter system. ITO contacts are particularly chosen because of their low resistance and excellent optical transmission properties. The system contains a central chamber which contains the ITO target and is evacuated by a turbo molecular pump. The plasma is formed by introducing pure argon and some 1% O_2/Ar gases excited by an Advanced energy plasma unit. The excited argon ions sputter the target and deposit ITO over the sample. A very thin nickel mask with predefined holes of 0.4 cm diameter is used to cover the sample for defining the ITO contacts. The thin mask avoids the edges of holes cutting into the active layers of the device and thus prevents electrical shorts. The sample is heated to 100 ºC and the pressure is maintained at 5 mT during deposition. A two minute pre-deposition is initially done for the plasma to stabilize followed by the actual deposition for 2.5 minutes while the applied DC bias is 20W.

3.5. Plasma Characterization by Quadruple Mass Spectroscopy

A quadruple mass spectrometer was hooked up to the reactor to study the dissociated radicals in the plasma. The set-up is as shown in Figure 3.18. Apart from the regular vacuum system for the reactor, the mass spectrometer was hooked with a separate vacuum system in order to establish very low pressures in the order of 10^{-8} required for the analysis. The main components of the spectrometer are the Ion detector, Ion filter and the Ionizer, together known as the Closed Ion Source (CIS) analyzer. In this mass spectrometer we have the option of switching the ionizer off if we need to eliminate the ions produced from the ionizer filament.

www.manaraa.com

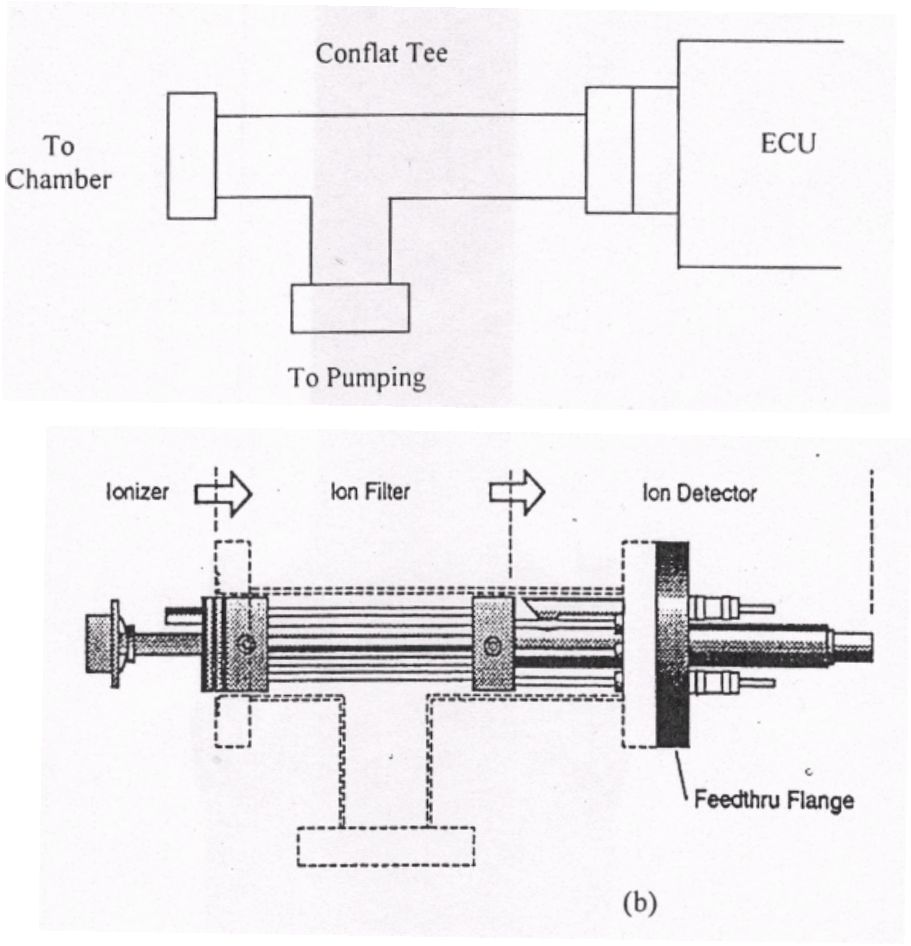

Figure 3.18: Quadruple Mass Spectrometer [56]

The main function of the ion filter is to separate the plasma ions based on their mass to charge ratio. The ions then travel to the detector which is basically a stainless steel Faraday cup. When the ions strike the metal wall of the cup, electrons are produced and thus an electrical current is generated. Finally the partial pressure of ions is evaluated by multiplying this current with the nominal sensitivity of the CIS analyzer. After every series of runs, the outer wall of the closed ion source analyzer was baked using a thermal jacket, to remove the absorbed species which can contribute significantly to the background signal in the subsequent runs.

www.manaraa.com

3.6. MESA Etching Technique to Pattern Device Contacts

3.6.1. Preclean

This is essential for proper adhesion of photoresist. Samples are boiled in acetone for 5 minutes and subjected to ultrasonic cleaning in methanol for 5 minutes. Then they are place in soft bake oven for 20 minutes at 90C do drive the moisture out of the sample

3.6.2. Image Reversal Photoresist

The first step is to spin the samples with AZ5214 photoresist for 40s at 4000rpm and then bake in oven at 100C for 4 minutes. The samples are then exposed with the mask for 72s and baked at 125C for 2 minutes. This step is very critical wherein the exposed regions undergo a phase transformation into an insoluble compound. Again they are exposed without any mask for 1.5 min and developed for about 60s in 31ZMIF, followed by a cascade rinse for 3 min and a hard bake in oven for 20 mins at 120C.

3.6.3. P+ Layer Etch

The etch solution contains, 30ml of Nitirc acid (Oxidises Si into SiO_2), 20ml of 50:1 Hydrofluoric acid (Etches away the SiO_2), 10ml of Acetic acid (Dilutant) and 90ml of water. The samples are carefully immersed into the etching solution. The actual etching time is for 40-45 seconds followed by a thorough rinse with distilled water for 5 minutes.

3.6.4. Photoresist Removal

To remove the photoresist protecting the contacts, the samples are again subjected to ultrasonic cleaning in acetone for 5 minute followed again by an ultrasonic in methanol for 1 minute. Finally they are baked in oven for 10 minutes at 175C.

www.manaraa.com

CHAPTER 4: RESULTS AND DISCUSSION

4.1. Effect of Hot Wire CVD Parameters on Grain Size and Orientation

In this section we study the influence of the some of the important deposition parameters like hydrogen dilution, substrate temperature and pressure on the structural properties of the film. Although there are literatures on the effect of these deposition parameters on crystallinity of the film, very few have actually reported the variation of grain size and orientation.

4.1.1. Effect of the Hydrogen Dilution

Hydrogen dilution is known as a very critical factor in increasing the crystalline fraction of the material. But in the fabrication of solar cells and other electronic devices, it is very important to know about the size of these crystalline grains and their orientation as they have a significant impact on the mobility of the carriers.

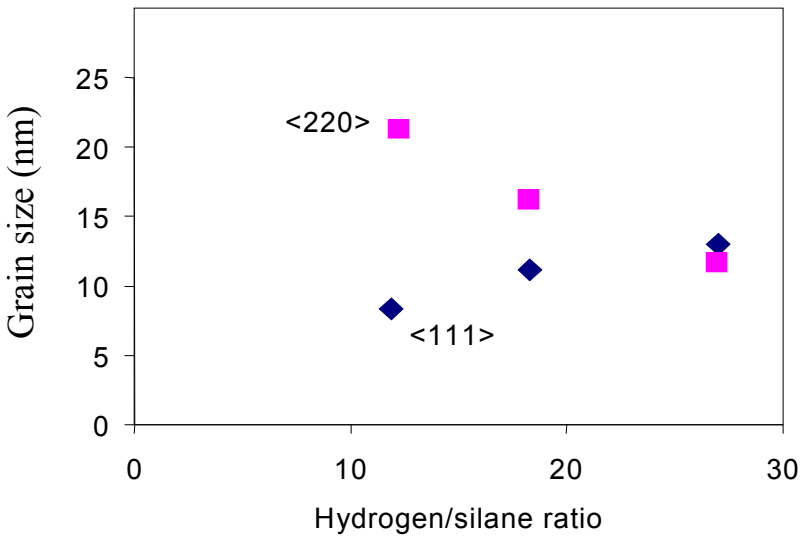

Figure 4.1: Grain size Vs Hydrogen/Silane ratio [57]

www.manaraa.com

Figure 4.1 shows the variation of grain size with different hydrogen dilutions. The deposition was done at a pressure of 5 mT and a substrate temperature of 300 ^{o}C. The filament temperature was about 1800 ^{o}C. The <111> grain size increases with the hydrogen dilution whereas the <220> decreases significantly. This is because the atomic hydrogen produced due to the thermal decomposition of silane, impinging the surface of the growing film, favors the grains due to random orientation and inhibit the thermodynamically favorable <220> grains [57]. If this is the case, then the intensity of <111> grains should be enhanced as we increase the hydrogen dilution. The following plot which gives the variation of <111>/<220> peak intensity ratio clearly reveals this trend. The intensity ratio increases linearly with the dilution ratio proving <111> grains to be dominant at higher dilutions.

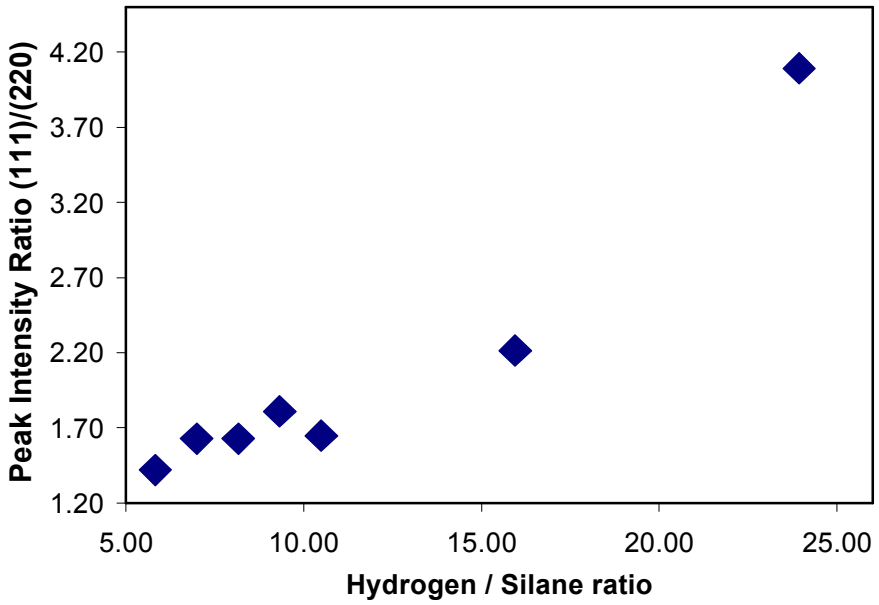

Figure 4.2: <111>/<220> intensity ratio Vs Hydrogen/Silane ratio

www.manaraa.com

4.1.2. Effect of Substrate Temperature

The substrate temperature has the same effect of hydrogen dilution in modifying the structural properties of the film. The material becomes more crystalline when the substrate temperature is increased. Thus, we would also expect the <111> grains to be the predominant orientation at higher temperatures. But the experimental results are contradictory to this trend as shown in Figure 4.3. The plot clearly shows the increase in <220> grain size when compared to that of <111> grains. All the depositions were done at 5mT using a single filament.

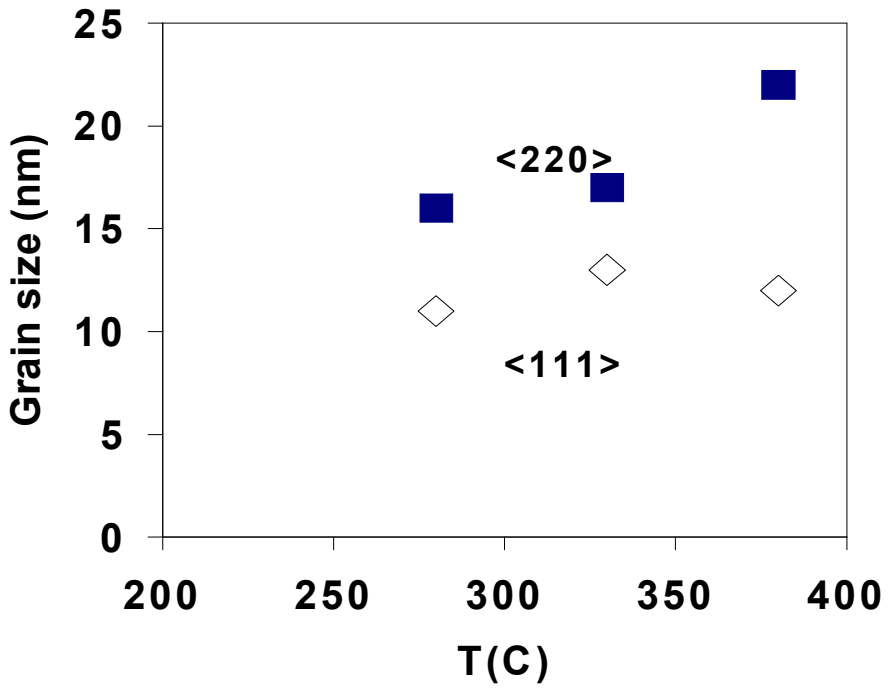

Figure 4.3: Grain size Vs substrate temperature [57]

When compared to the <111> orientation, <220> has a higher surface energy [58]. This means that when the substrate temperature is high, which is a thermodynamically favorable condition, the <220> grain size should be enhanced. A similar result has also been

www.manaraa.com

reported by Jones et al. for TiN coatings by reactive RF sputtering [59]. They concluded that the increase in substrate temperature has a significant influence in enhancing the surface mobility of the deposited atoms which finally results in a more stable structure which is of <220> orientation. The influence of substrate temperature was also explored at higher hydrogen dilutions. Ideally, the <220> grains should be suppressed at higher hydrogen dilutions and increased temperatures should have the reverse effect. Our experimental results for various hydrogen dilution ratios as shown in Figure 4.4, revealed that the substrate temperature has a more direct control over the <220> grains, at least till a reasonably high dilution ratio of 16:1.

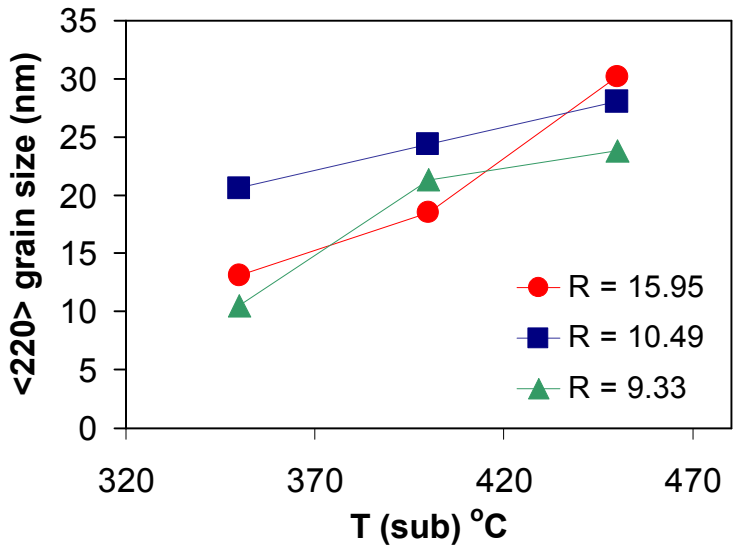

Figure 4.4: <220> grain size Vs temperature for different Hydrogen/Silane ratios

4.1.3. Effect of Chamber Pressure

When compared to the substrate temperature and the hydrogen dilution, chamber pressure has the opposite effect on the crystalline ratio of the material. As the deposition pressure is increased, the mean free path between the radicals decreases with a significant

www.manaraa.com

increase in the average number of collisions between them. This promotes more secondary reactions to occur between the gaseous species and also considerably reduces the flux of hydrogen radicals required to induce crystallization. Thus the material tends to become amorphous at very high deposition pressures.

Figures 4.5 and 4.6 show the variation of grain size and orientation with changes in chamber pressure. The depositions were done using a filament temperature of ~1800 ^{o}C and a substrate temperature of 250-300 ^{o}C. It can be seen that the <220> grains significantly increase with the pressure, while the <111> grains get suppressed at higher pressures. At low pressure, there is relatively high concentration of atomic hydrogen when compared to the silyl radicals which are considered to be the growth precursors.

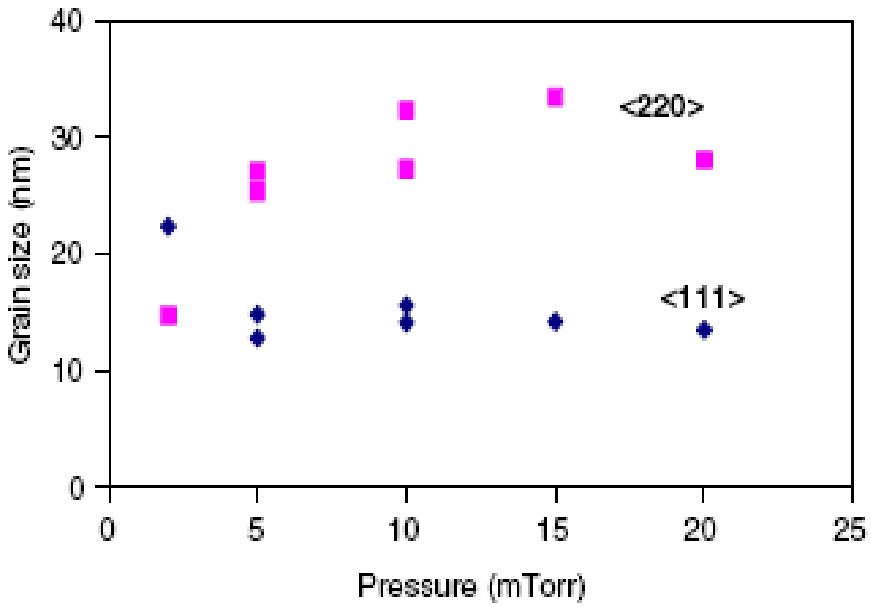

Figure 4.5: Influence of chamber pressure on grain size [60]

This promotes random nucleation in the growing film and thus the <111> grains are relatively enhanced when compared to that of <220> grains. But at higher pressures, the

www.manaraa.com

concentration of atomic hydrogen to silyl radical decreases significantly which reduces random nucleation and promotes the <220> grains. Also, at higher pressures we obtained high growth rates strongly confirming the increased concentration of silyl radicals.

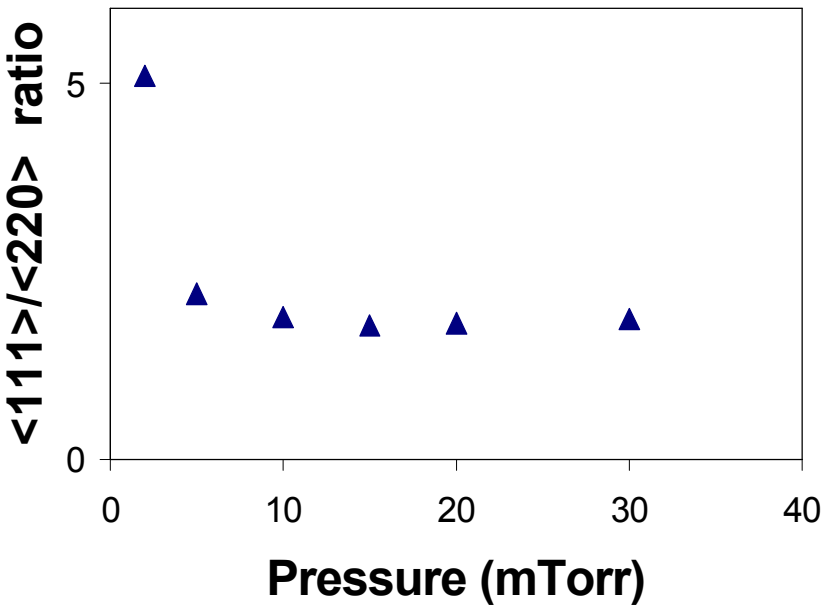

Figure 4.6: Peak intensity ratio Vs Chamber pressure [57]

4.2. Effect of Helium Addition in HWECR and HWCVD

In this section, we report the effect of helium ions on the crystalline properties of the films deposited using combined hot wire and ECR CVD techniques. We later compare these structural properties with films made from hot wire only to isolate the effect of plasma ions.

4.2.1. Effect of the Incident Microwave Power

Figure 4.7 shows that the crystalline ratio of the deposited films increases with the plasma power in the presence of helium, hydrogen and silane. The crystalline films were

www.manaraa.com

grown at 10mT and at a substrate temperature of 300 ^{o}C. The helium dilution ratio in hydrogen was kept constant at 0.5:1.

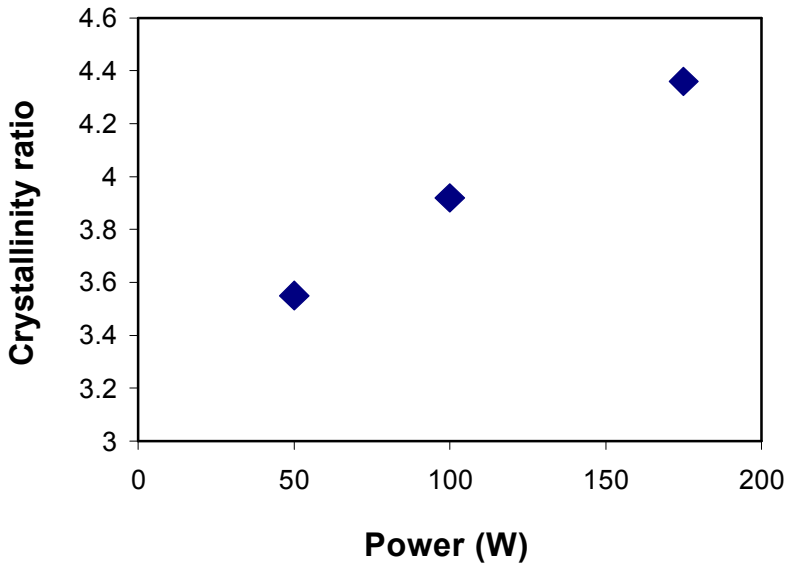

Figure 4.7: Effect of applied power at constant helium dilution

Dalal had explained the role of helium very clearly in one of his earlier works [16]. He stated that helium ions from the plasma are very efficient in removing the surface H atoms and thus leave very low concentration of clustered H in the deposited film. He also stated that the hydrogen ions apart from removing the H atoms from broken bonds on the surface, also penetrate deep in to the film to remove the weekly bonded H atoms, thus improving the microstructure of the film. Veprek showed that the deposition of microcrystalline silicon under low chamber pressure is a result of the competition between etching (removal of bonded hydrogen) and the deposition [61]. Thus when the applied power increases, more helium and hydrogen atoms get ionized and more surface hydrogen bonds are broken and removed. This improves the etching efficiency and as a result the material becomes more crystalline.

www.manaraa.com

4.2.2. Effect of Helium Dilution Ratio

Since the helium and hydrogen ions enhance the film crystallinity, one would expect the crystalline properties to improve when the helium dilution ratio is also increased. But Figure 4.8 proves that the helium concentration has a negative effect on the crystalline ratio of the deposited films.

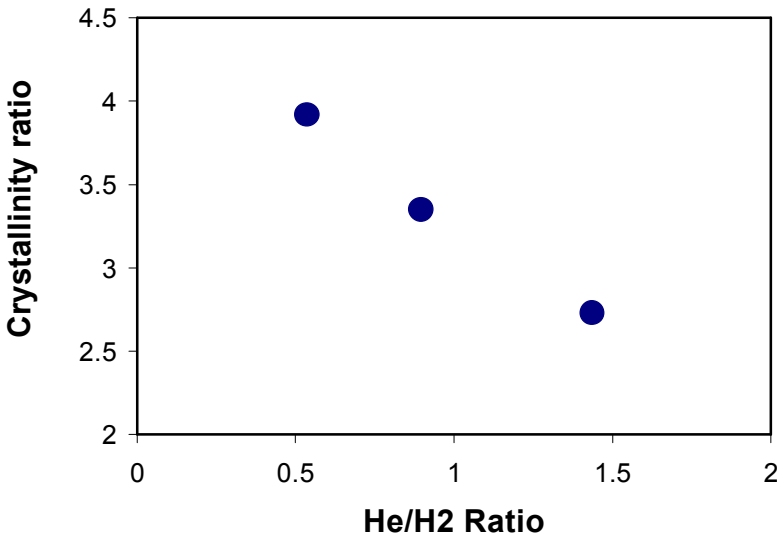

Figure 4.8: Raman ratio Vs helium dilution

According to Veprek, the rate of etching by plasma ions and the rate of deposition of silicon will yield a quasi-equilibrium state that is energetically favorable for the formation of a thermodynamically stable microcrystalline material [61]. But if there are too many helium ions or atoms, they can easily disturb the equilibrium established on the growing surface when they bombard the surface with an energy of ~6eV which may be too energetic for the formation of microcrystalline material. Also, when there is a high concentration of helium ions, they can prevent hydrogen ions from penetrating into the subsurface of material which is critical for removing the broken bonds and re-structuring the network.

www.manaraa.com

4.2.3. Effect of Plasma Ions in Combined Hot Wire and ECR CVD Depositions

By depositing films under identical conditions in both hot wire and combined hot wire ECR techniques, we were able to isolate the effect of plasma ions in modifying the structural property of the films. The results are plotted in Figure 4.9. It can be seen that the crystalline ratio of the material is low around 0.6, when we use the SiH4/H2 mixture in HWCVD. But under identical conditions, when we just add 50W or 100W of plasma power, ions are generated and the crystalline ratio shows a sharp increase to ~4.0. This explains the importance of plasma ions in removing the weakly bonded hydrogen both from the growing surface and subsurface.

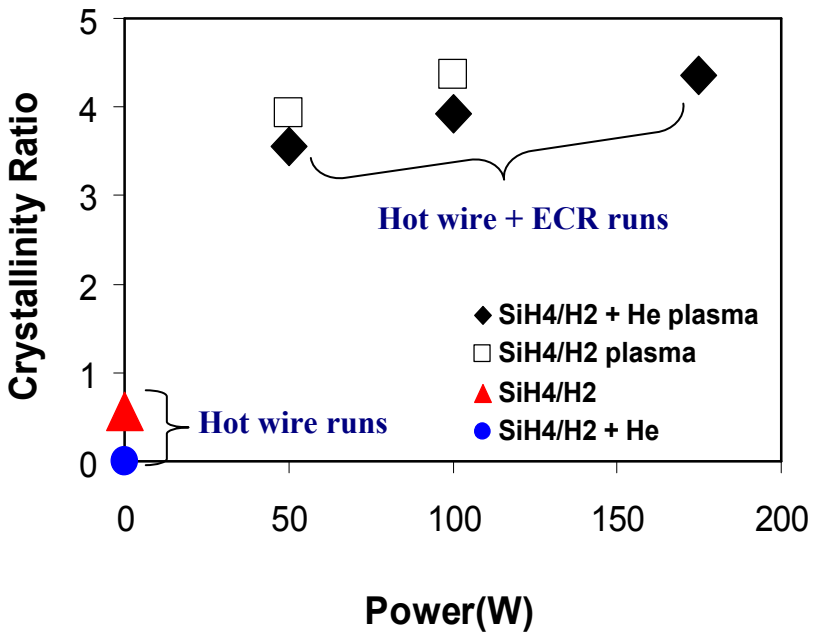

Figure 4.9: Effect of plasma ions

In HWCVD since there are no ions present, the efficiency of this bonded H removal process is low which also affects the crystallinity of the material. When we add helium to the mixture in HWCVD, the film becomes completely amorphous. The reason for this could be

www.manaraa.com

the bombardment of heavy helium atoms on the growth surface, completely disturbing the equilibrium state necessary for the formation of the microcrystalline phase.

To study the influence of radicals and ions on grain orientation, we compared the XRD results for both HWECR and HWCVD. The results are as shown in Figure 4.10. The plasma power corresponding to 0W refers to the hot wire runs. The plot clearly shows that the <220> grains are enhanced and the <111> grains are suppressed in the hot wire deposition where there are no plasma ions. But once when the plasma is turned on, the <220> grains are significantly suppressed and the <111> grains become the dominant ones. Since the nanocrystalline silicon deposition is comprised of an etching component and a deposition component, the growth rate of the films should be reduced in the presence of plasma ions which can enhance the etching component. This is exactly what we observed using our combined hot wire ECR runs as shown in Figure 4.11.

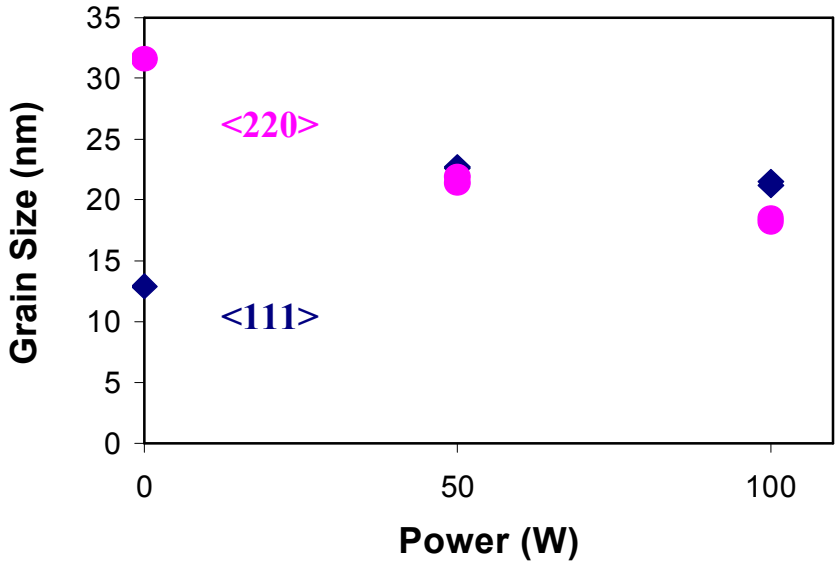

Figure 4.10: Comparison of <111> and <220> grain size for HWECR and HWCVD

www.manaraa.com

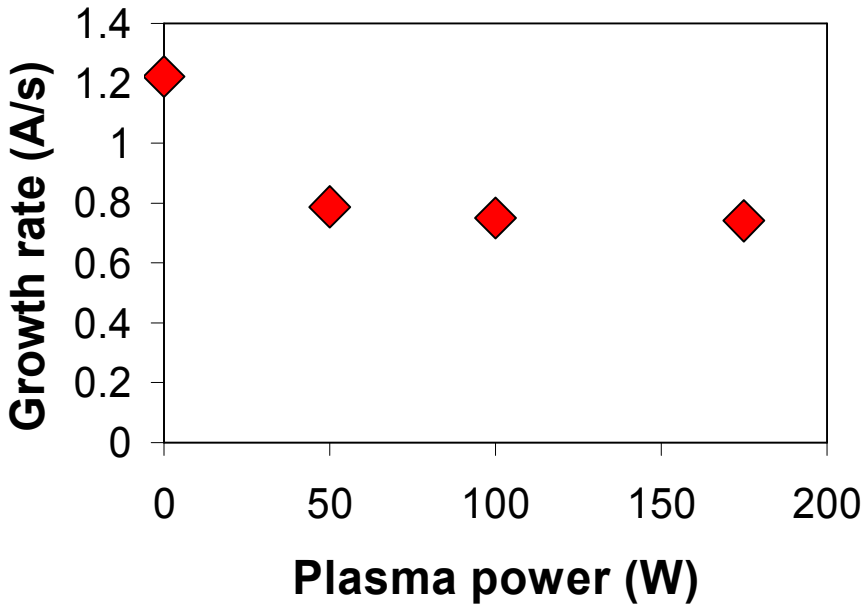

Figure 4.11: Influence of plasma ions on the film growth rate

4.3. Detection of Growth Radicals Using Quadruple Mass Spectrometer

We also studied the dissociation of silane into different ions under the influence of remote ECR plasma. Experiments were done for both nanocrystalline and amorphous silicon deposition conditions. It is believed that SiH_3 is the dominant radical in a plasma discharge for both amorphous and nanocrystalline silicon growth. But based on our plasma diagnostics, we found out that SiH is the dominant species in case of nanocrystalline silicon growth and SiH_2 is the dominant one in amorphous silicon deposition.

Figure 4.12 was obtained for a 10:1 hydrogen dilution and at a pressure of 2 mT. It is evident from the plot that for a wide range of plasma power starting from 50W to 250W, SiH is the most dominant radical. This is a very interesting result as most of the groups argue that SiH_3 is the dominant radical and also the primary growth precursor under plasma dissociation

www.manaraa.com

of silane. In fact Kondo et al., concluded that the primary dissociation of silane results in SiH_3 because of the lowest threshold energy of 8.73 eV as shown in Fig. 2.19 [41].

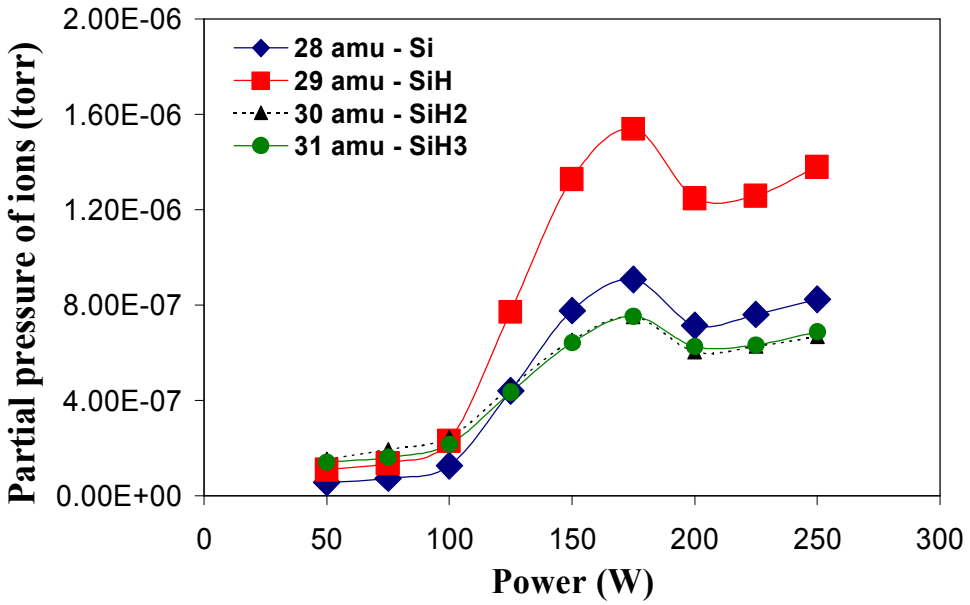

Figure 4.12: Dominant radical for nanocrystalline growth conditions

M. Pontoh from our group, had already shown that the film precursor is produced at a rate equal to the production of SiH by correlating the growth rates of the deposited films, Optical Emission Spectroscopy counts of SiH and the mass spectroscopy results [56]. Thus the results are consistent with SiH being the dominant species for the growth of nanocrystalline silicon.

Figure 4.13 shows the dissociation pattern for a wide range of chamber pressure and for a-Si deposition conditions. The applied power was 100W with 30% He and 20% SiH4. The plot shows that the dominant ions during the a-Si deposition are SiH2 and SiH3. This result is consistent with Veprek's theory for a-Si plasma induced deposition [62, 63].

www.manaraa.com

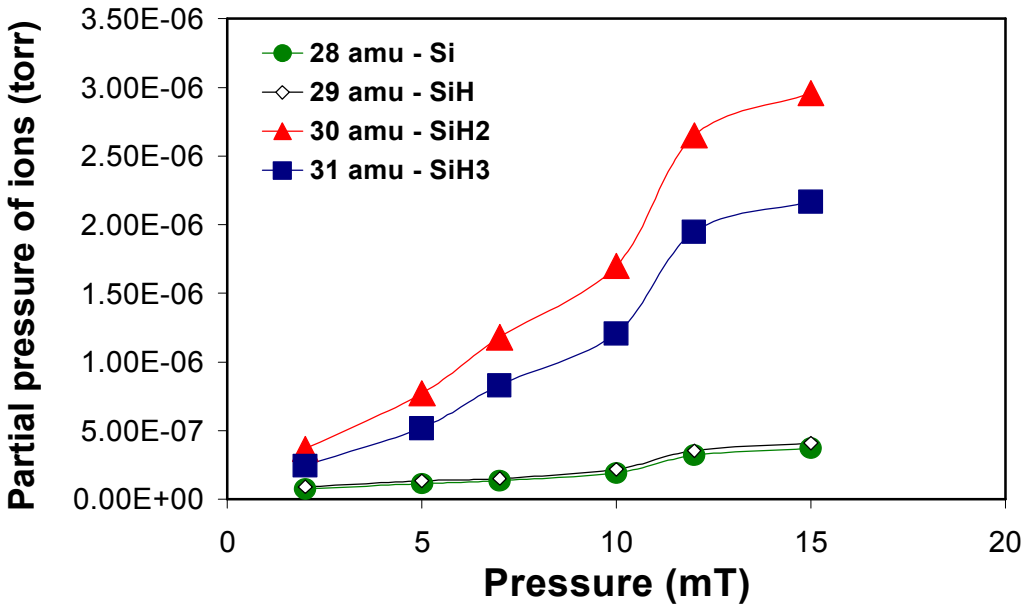

Figure 4.13: Variation of partial pressure of ions with chamber pressure

Through a self-consistent analysis of kinetic data for radical reactions, Veprek et al., were able to propose the following mechanism for a-Si deposition,

$$SiH_4 \longrightarrow SiH_2 + H_2 \quad (4.1)$$

$$SiH_2 + SiH_4 \longrightarrow Si_2H_6 \quad (4.2)$$

$$SiH_2 + Si_2H_6 \longrightarrow Si_3H_8 \quad (4.3)$$

According to them, the fragmentation of silane into SiH2 and H2 and the consequent fast insertion reactions (4.2) and (4.3), are the dominant reactions for a-Si deposition. Based on their analysis, they argue that SiH_3 radical would play only a negligible role in the film deposition. Gallagher had postulated that the actual branching to various products will depend on the pressure and SiH_4/H_2 ratio [40].

www.manaraa.com

The above results clearly suggest that, the dominant radical for different growth conditions need not necessarily be SiH_3 due to its low dissociation energy when compared to the other radicals. The dissociation pattern is strongly dependant upon the deposition parameters which can significantly influence the growth precursors generated during the actual deposition. It will be very useful to study the dissociation pattern in HWCVD and HWECR since the deposition conditions are quite different than that of the regular ECR PECVD.

4.4. Process and Design Optimization of Nanocrystalline Solar Cell Devices

In order to obtain high efficiency devices with good electrical characteristics, we had to optimize some of the design parameters and also the post treatment methods. The factors which made a significant improvement in our device properties are discussed here in detail.

4.4.1. The MESA Etch Technique

Some of the devices which had good I-V characteristics gave unreasonably high defect densities when characterized using our C-V technique. We speculated that those samples were highly crystalline so that there was significant conductance in the lateral directions which altered the capacitance values in the C-V experiments. We adopted the MESA etch technique described in the experimental section, to pattern the contacts. Figure 4.14 shows the schematic of the device before and after MESA etch. The leakage in the lateral direction is indicated as red arrow marks. It can be seen from the plot that for devices after MESA etch, the area under the ITO contacts are properly defined and free from the leakage effects. This reduced the capacitance values significantly and ultimately the defect

www.manaraa.com

density values were also lowered. The effect of MESA etch can be seen from the following ANOVA plot which compares the defect densities of the devices both before and after the treatment.

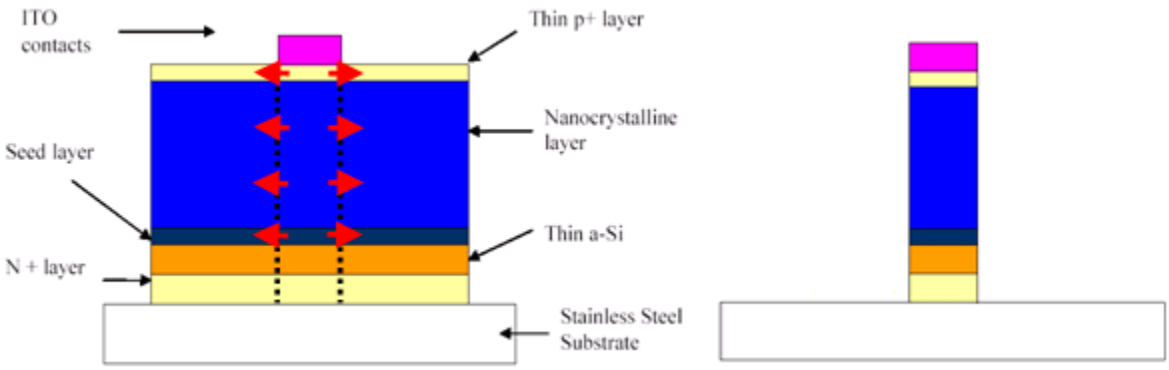

Figure 4.14: Device structure before and after MESA etch

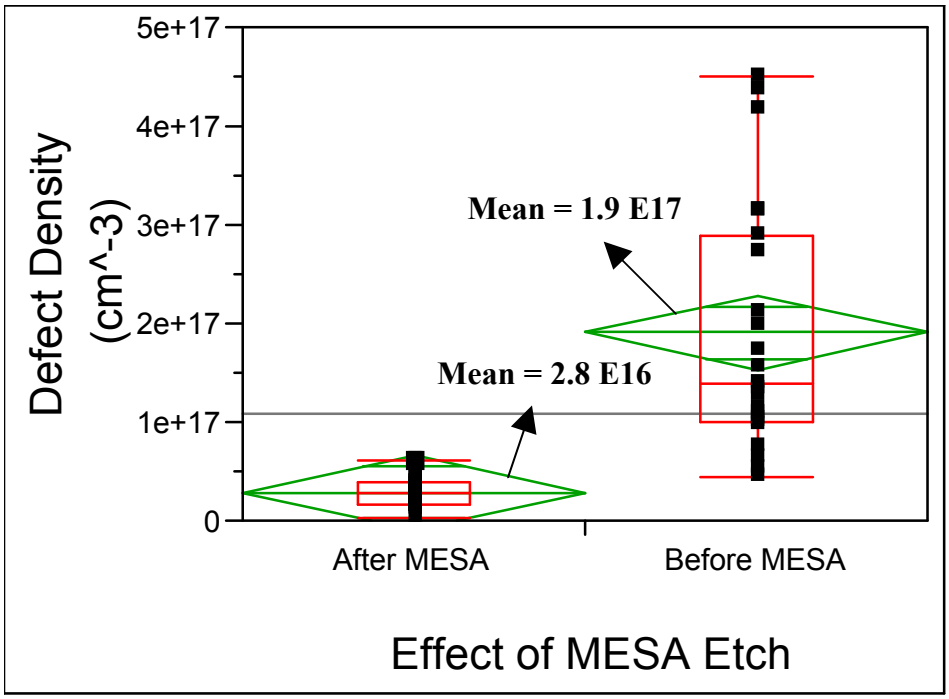

Figure 4.15: One-way ANOVA for effect of MESA etch

www.manaraa.com

It is evident from the variance analysis that the defect density had reduced by approximately an order of magnitude because of the etching technique.

4.4.2. Effect of Post Thermal Annealing

The devices showed significant improvement in their I-V characteristics after post thermal annealing for 60-90 minutes at 175 °C. The results are shown in Figure 4.16 and the corresponding change in electrical characteristics is given in Table. 4.1. The table shows that the series resistance decreases significantly for longer times of annealing. This is because the ITO contacts form good interface with the topmost p+ layer of the device at elevated temperatures. Also thermal annealing can relaxe the network by clearing off some of the weak bonds which reflects as an improvement in the other electrical characteristics as well.

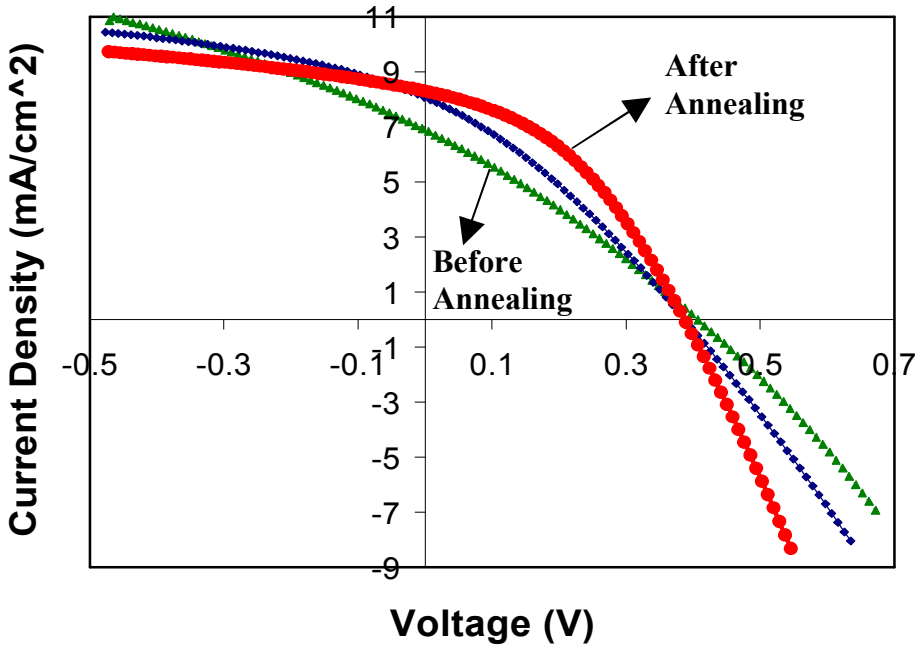

Figure 4.16: Effect of thermal annealing on the device I-V characteristics

www.manaraa.com

Annealing time (min)	R_S (ohms)	R_{Sh} (ohms)	I_{SC} (mA)	V_{OC} (V)	F. F (%)
0	347	760	0.86	0.41	29
15	260	961	1	0.39	32
90	157	1755	1.04	0.39	41

Table 4.1. I-V characteristics after different annealing times

4.4.3. Effect of Boron Grading

During the intrinsic layer deposition, boron was added to compensate for unintentional doping by oxygen and also to establish the electric field profile which can aid in better carrier transport as described in the experimental section. Based on our device results, we found out that the rate at which boron is graded also plays a huge role in improving the device properties. The boron concentration was increased slowly during the deposition of the i-layer till about two-thirds of the layer thickness. The different grading times refer to the interval between successive increase in the gas flow rate. Figure 4.17 shows a significant improvement in I-V characteristics for the devices subjected to boron grading. It can also be seen that the 2 min boron grading has a greater impact on the I-V characteristics than when compared to that of 10 min grading because of the smoother electric field in the former case. Figure 4.18 shows the band diagram of the device with boron grading. As shown in the figure, the boron grading induces only a very little band bending in the intrinsic layer.

www.manaraa.com

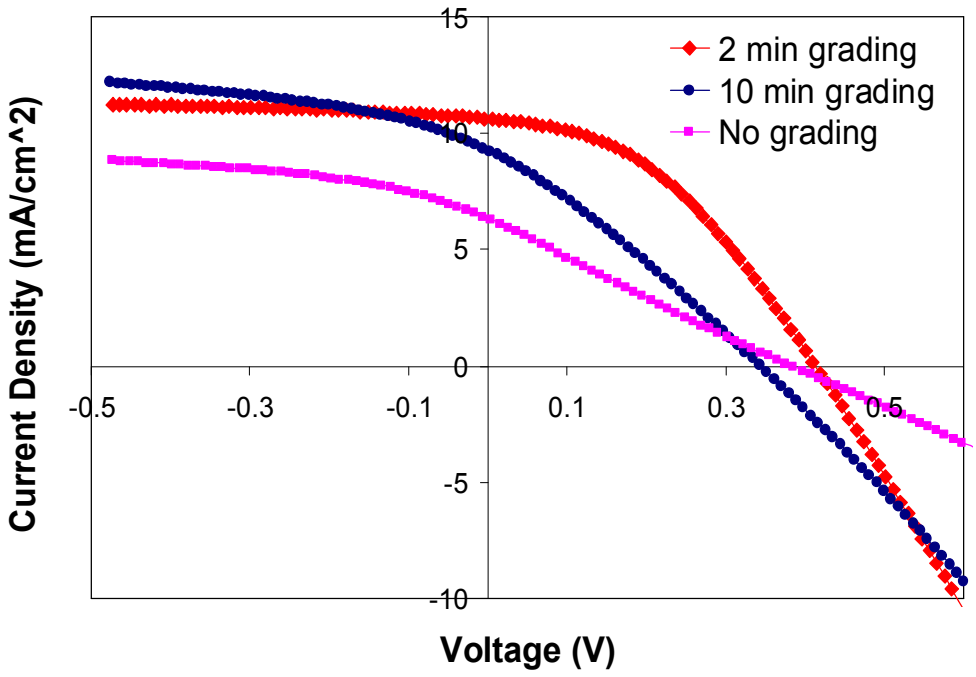

Figure 4.17: Effect of boron grading on I-V characteristics

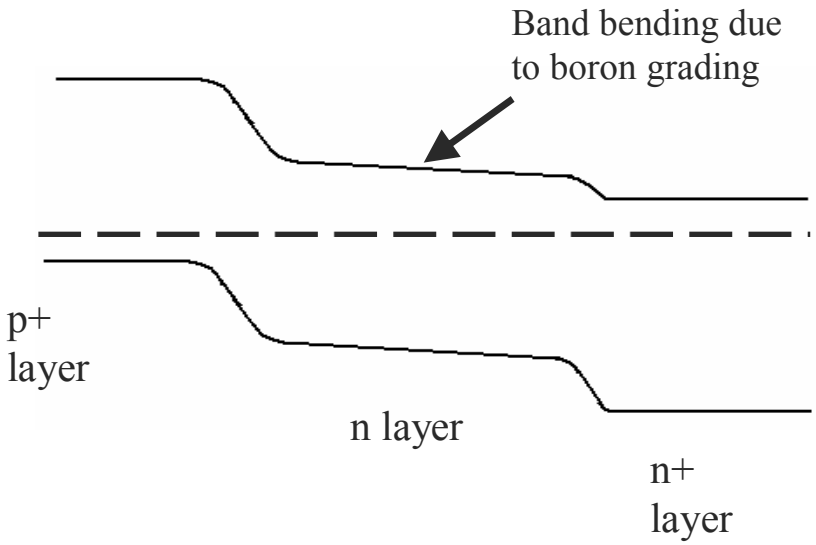

Figure 4.18: Influence of boron grading

www.manaraa.com

The following calculation roughly shows how this helps in carrier transport. We know that, under the influence of electric field, the range for the minority carriers is given by,

$$R_P = \mu\tau E \tag{4.4}$$

For nanocrystalline silicon, $\mu \sim 1 cm^2/V\text{-}s$ and $\tau \sim 1$ μs. Assuming $R_P = 5$ μm, the electric field is evaluated to be 5×10^2 V/cm. Then the required band bending for a 1 μm base layer is 0.05 eV. Thus the preliminary calculations reveal that a small amount of band bending induced by the boron grading, significantly improves the transport properties of the minority carriers.

4.5. Results on Nanocrystalline Solar Cells

In this section we will discuss the effect of growth conditions on the properties of devices fabricated by both hot wire and combined hot wire and ECR CVD techniques.

4.5.1. Why Transition Region for High Efficiency Devices?

The high efficiency solar cell devices are being fabricated in a region close to the transition to amorphous phase. In order to explore the importance of transition region, we have systematically studied the critical properties like diffusion length of the minority carriers, defect density and the quantum efficiency by fabricating devices with intrinsic layers of varying crystalline fractions. In Figure 4.19 we show the variation of diffusion length and defect density of the solar cells with intrinsic layers of different crystallinity. The diffusion length increases as the crystalline ratio is decreased and after reaching a peak value

www.manaraa.com

of about 1.7 µm, it decreases sharply for crystalline ratio less than 2.0. The defect density follows exactly the opposite trend reaching a minimum value at a crystalline ratio of 2.0.

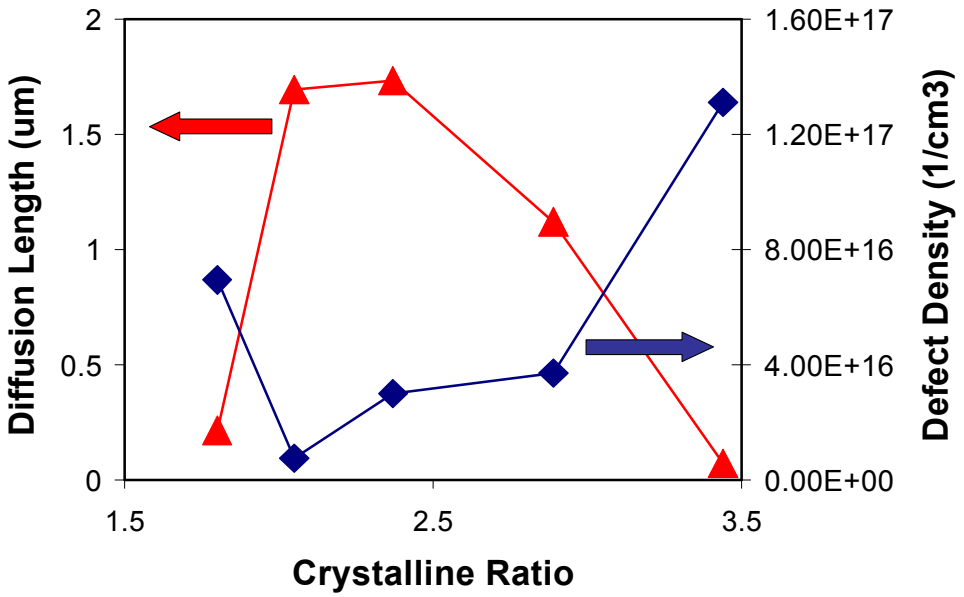

Figure 4.19: Correlation of electrical properties with structural properties

Figure 4.19 is a very important plot in understanding the importance of the transition region between amorphous and crystalline phase. We know that the nanocrystalline intrinsic layer contains crystalline grains surrounded by amorphous tissues which are very effective in passivating the grain boundaries thus enhancing the transport of the generated carriers. For highly crystalline samples with very less amorphous tissues the carrier transport is hindered due to inefficient passivation resulting in poor diffusion lengths and the defect densities are also high due to the porous texture of the material that allows diffusion of atmospheric species when exposed to ambient air [30,33]. On the other hand, samples of very low crystalline ratios have bulky amorphous tissues which significantly increase the defect

www.manaraa.com

density and also increase the barrier height at the grain boundaries hindering efficient carrier transport. If this reasoning is true, then we should also have enhanced carrier collection at the transition region. The results from the quantum efficiency measurements as shown in Figure 4.20, exactly follow this trend further signifying the importance of the transition region.

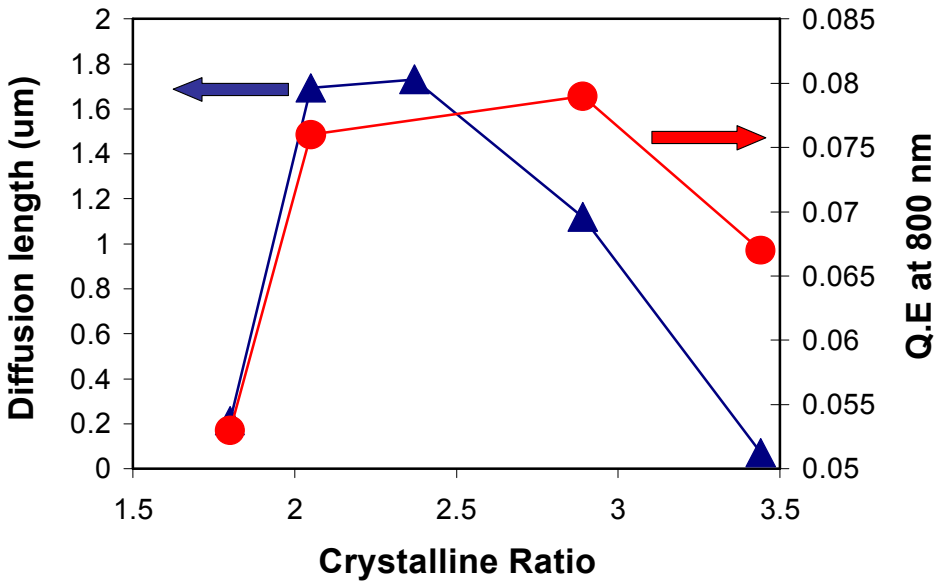

Figure 4.20: Variation of carrier collection at 800 nm with crystalline ratio

4.5.2. Effect of Filament Temperature

In the above experiments, the crystalline ratio of the intrinsic layer was varied by changing the hydrogen dilution ratio. The other critical knob to change the crystalline property of the film is the filament temperature. Figure 4.21 shows the variation of diffusion length and the quantum efficiency for various filament temperatures. The filament temperature and the hydrogen dilution ratio are closely linked in a way that both have the same influence on the crystalline ratio. At very low filament temperatures the sample is

www.manaraa.com

mostly amorphous leading to low diffusion length, because a low filament temperature does not decompose hydrogen efficiently. High filament temperatures results in an increased concentration of atomic hydrogen, that makes the sample highly crystalline. Thus the observed trend for filament temperature variation is same as that of hydrogen dilution.

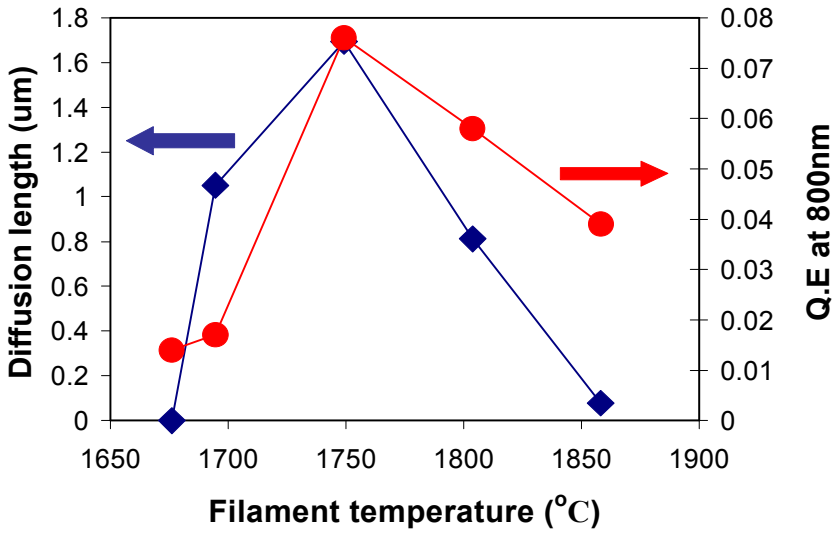

Figure 4.21: Effect of the filament temperature on the device electrical properties

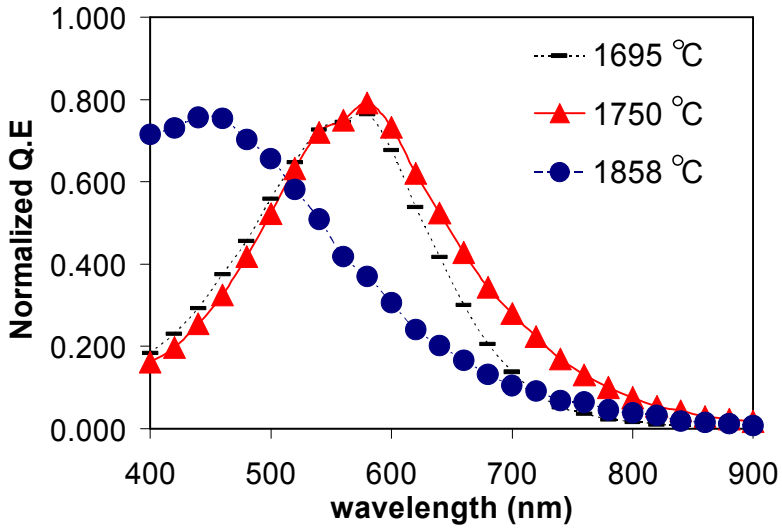

Figure 4.22: Quantum efficiency spectra for different filament temperatures

www.manaraa.com

We also compared the overall quantum efficiency spectra to see the influence of filament temperature. The results are plotted in Figure 4.22. The plot clearly indicates a broad spectrum at moderate filament temperature and comparatively low quantum efficiencies for both high and low temperatures. The spectrum is significantly shifted to very low wavelengths for high filament temperatures. In Figure 4.23 we compare the I-V characteristics of the device fabricated with different filament temperatures.

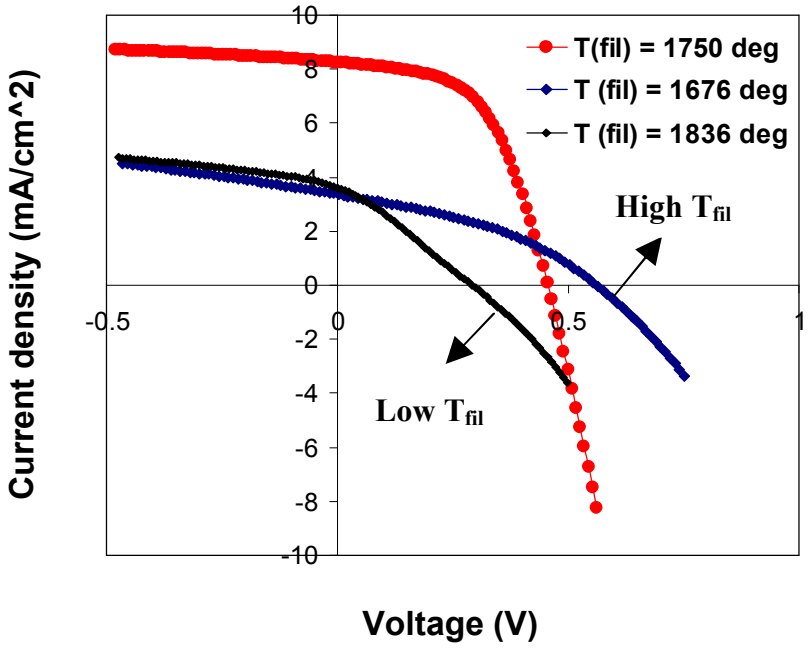

Figure 4.23: I-V characteristics at different filament temperatures

The electrical characteristics strongly suggest that both low and high filament temperatures are detrimental to the growth of high efficiency solar cells.

4.5.3. Effect of Chamber Pressure

Although studies have been done on the influence of deposition pressure on the properties of the nanocrystalline film, virtually no work has reported the direct effect of

www.manaraa.com

pressure on the device properties such as diffusion length and quantum efficiency. It was shown earlier that increase in pressure, increases the bonded hydrogen content and also the oxygen concentration in pores [31]. In this section we show how the device properties are affected by varying the chamber pressure.

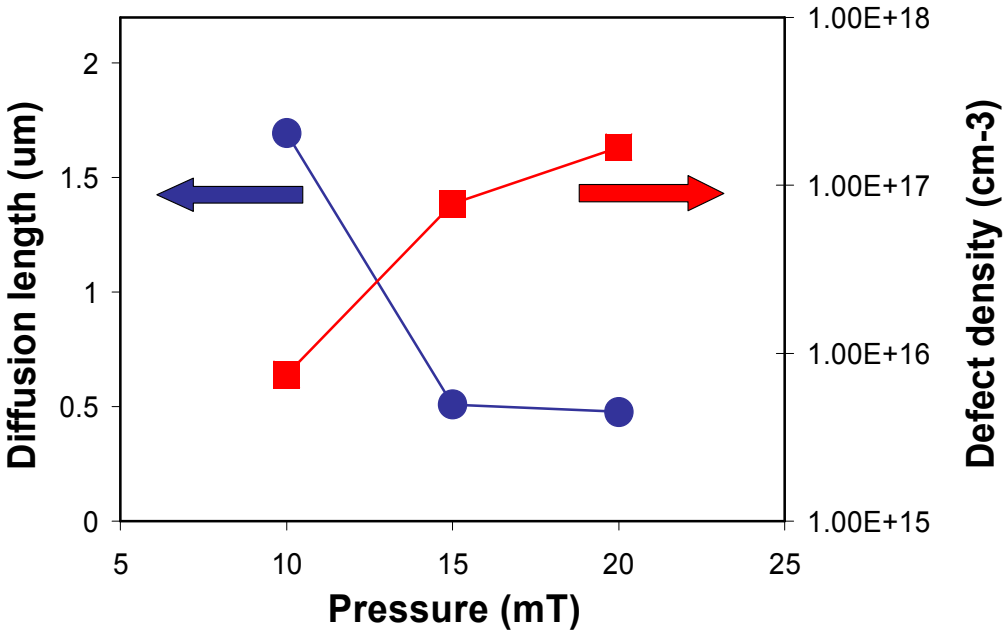

Figure 4.24: Influence of chamber pressure on diffusion length and defect density

Figure 4.24 clearly shows that at high deposition pressures, the defect density increases by over an order of magnitude thus significantly reducing the diffusion length of the minority carriers. In the following plot we show the effect of pressure on the carrier collection efficiency at longer wavelengths. The broad spectrum and the increased quantum efficiency at longer wavelengths strongly suggest that low deposition pressure is ideal for fabricating good quality devices. It can also be seen that the collection efficiency decreases significantly at higher pressures.

www.manaraa.com

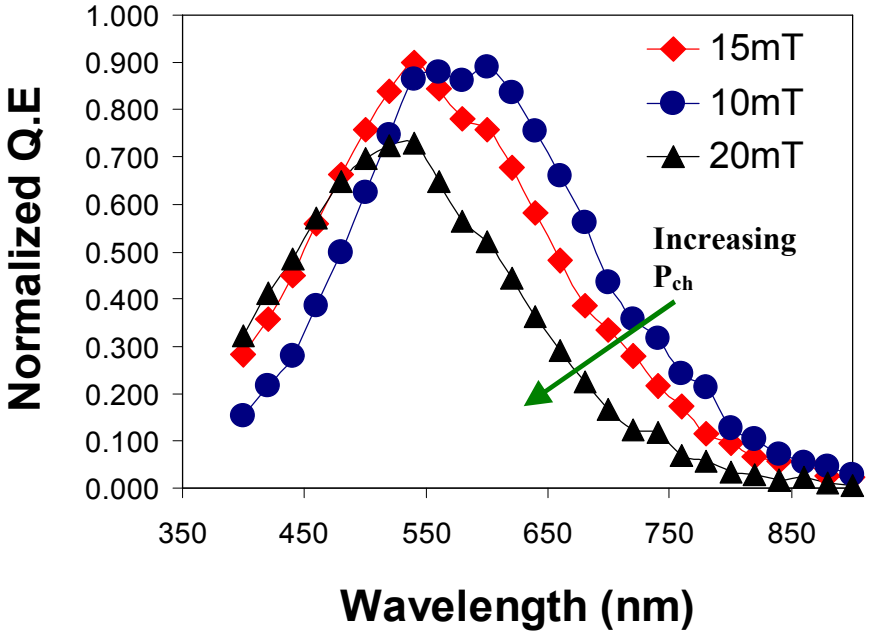

Figure 4.25: Quantum efficiency spectra at different chamber pressures

4.5.4. Results on Devices from Combined Hot Wire and ECR CVD Techniques

The devices fabricated from the combined hot wire and plasma techniques also exhibited the same trend, wherein devices made at both high and low filament temperatures had very low short circuit current density. The results are plotted in Figure 4.26. All the devices were fabricated with a incident plasma of 50W, at a chamber pressure of 10mT and at a substrate temperature of 250 °C. The increase in V_{OC} at lower filament temperatures suggests that the intrinsic layer is becoming more amorphous. The drastic decrease in the short circuit current at both low and high filament temperatures, directly signifies that the transport properties of the photogenerated minority carriers are being affected which might be due to the change in structural properties of the intrinsic layer. More studies can be done to investigate the change in diffusion length and the defect densities with the variation of

www.manaraa.com

plasma power and hydrogen dilution ratio in this combined hot wire and ECR technique. By correlating the results with the hot wire technique, the influence of adding plasma ions in improving the device efficiency can also be explored.

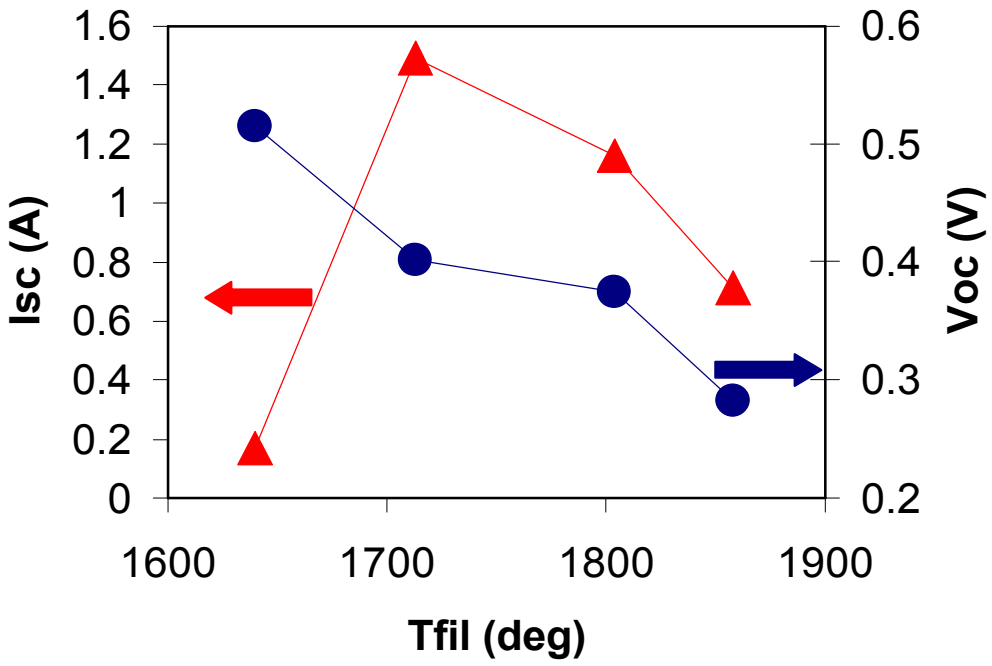

Figure 4.26: Effect of filament temperature on devices made by combined hot wire and ECR CVD techniques

www.manaraa.com

CHAPTER 5: CONCLUSIONS

To conclude, its been successfully shown that the deposition conditions during HWECR or the HWCVD can have a strong influence on the structural properties of the film by changing the grain size and also the preferred orientation along <111> or <220>. To understand the importance of the so-called 'transition region' in obtaining high efficiency solar cells, the electrical properties of the nanocrystalline devices were studied systematically. The main properties explored apart from the regular I-V characteristics were the minority carrier diffusion length, defect density and the quantum efficiency. The variation of these critical properties, were correlated with the structural properties of the intrinsic layer. The significant results are as follows;

- The atomic hydrogen produced due to thermal decomposition of silane on the hot-wire, has the same effect of hydrogen ions in plasma, to induce random nucleation in the film. Hence the <111> grains are enhanced when the hydrogen dilution ratio is increased in the hot wire technique. Both substrate temperature and chamber pressure enhance the thermodynamically favorable <220> grains, although at very high pressures the film becomes completely amorphous.

- The influence of applied power and helium dilution on the crystallinity of HWECR films was studied in detail. It was concluded that when the applied power increases, more helium and hydrogen atoms get ionized and more surface hydrogen bonds are broken and removed. This improves the etching efficiency and as a result the material becomes more crystalline. On the other hand when the helium dilution was increased, the crystallinity decreased, indicating that the energetic helium ions striking the growing film surface,

www.manaraa.com

may disturb the quasi-equilibrium which is critical for the formation of microcrystalline phase. Helium ions can also prevent the hydrogen ions from penetrating into the film to break the weak bonds and abstract excess hydrogen.

- The HWECR and HWCVD films were compared to show the critical role of the plasma ions in the deposition of nanocrystalline silicon. The crystalline ratio of the material was low around 0.6, when SiH4/H2 mixture was used in HWCVD. But under identical conditions, when a little plasma power of 50W was added, the crystalline ratio increased drastically to ~4.0. The growth rates decreased significantly in the presence of plasma ions. The results proved that the plasma ions are very efficient in removing the hydrogen from the broken bonds, thus increasing the etching component to form a highly crystalline material at a reduced growth rate.

- The fragmentation pattern of silane in ECR PECVD was studied in detail using a quadruple mass spectrometer. The study revealed the dominant radicals in both nc-Si and a-Si depositions for varying power and chamber pressures. It was found out that SiH was the dominant radical for nc-Si deposition, but SiH_2 became the dominant one for a-Si deposition. The identification of SiH as the dominant radical in nc Si deposition is a new result which contradicts all previous assumptions about which radical is important for the growth of nano Si, at least at low pressures. The results strongly suggested that the dissociation pattern is dependant upon the deposition conditions, which can significantly influence the growth precursors generated during the actual deposition.

- From the nanocrystalline device results, it was evident that the diffusion length increased as the crystalline ratio was decreased and after reaching a peak value of about 1.7 μm, it

www.manaraa.com

decreased sharply for crystalline ratios less than 2.0. The defect density followed exactly the opposite trend, decreasing by over an order of magnitude and reaching a minimum value at a crystalline ratio of 2.0. The results proved that very high and very low crystalline ratios are both detrimental to the growth of good quality nanocrystalline devices.

- The effect of filament temperature and the chamber pressure on the device electrical properties was also explored. Based on the final results it was concluded that high efficiency devices with low defect density and high diffusion length can only be obtained at a moderate filament temperature and low chamber pressures. The I-V characteristics and the quantum efficiency spectra of the corresponding devices further validate these conclusions.
- The effect of MESA etch in patterning the device contacts, the influence of boron grading rate and the post thermal annealing in improving the device properties were also discussed in detail. It was shown that to obtain true results, one must use a mesa structure.

www.manaraa.com

FUTURE RESEARCH DIRECTIONS

- The influence of deposition conditions like hydrogen dilution, substrate temperature and chamber pressure on grain size and orientation using combined HWECR CVD can be studied systematically. The results can be compared with that of HWCVD films to further explore the advantages of HWECR technique.

- Having known the influence of HWCVD deposition conditions on the structural and electronic properties of devices and the effect of plasma ions in HWECR films, the next step would be to study the variation of critical electronic properties like the diffusion lengths and the defect densities in the presence of ECR plasma ions.

- The mass spectroscopy studies can be extended to HWECR and HWCVD depositions to explore the dominant radicals responsible for good quality nc-Si films. In HWCVD, it is very difficult to detect the species using quadruple mass spectroscopy, since there are no ions generated during the process. A normalization experiment can be performed to isolate the effect of hot wire radicals by comparing the mass spectra of HWECR and ECR, or the ionization voltage of the ionizer filament can be fine tuned to detect the desired species.

www.manaraa.com

REFERENCES

[1] K. Yamamoto, M. Yoshimi, Y. Tawada, Y. Okamoto, A. Nakajima, S. Igari, Appl. Phys. A. **69** (1999) 179

[2] S. Klein, F. Finger, R. Carius, B. Rech, L. Houben, M. Luysberg, M. Stutzmann, in: J.D. Cohen, J.R. Abelson, H. Matsumura, J. Robertson (Eds.), Amorphous and Heterogeneous Silicon-Based Films Materials, San Francisco, USA, 2– 5 April 2002, Research Society Symposium Proceedings, vol. 715, 2002, p. 617

[3] Alan L. Fahrenbruch and Richard H. Bube, "Fundamentals of Solar cells", Academic Press Inc. (London), 1983

[4] J. Zimmer, H. Stiebig and H. Wagner, J. Appl. Phys. **84**, (1998) 611-617

[5] M. Sendova-Vassileva, S. Klein, F. Finger, Thin Solid Films **501**, (2006) 252-255

[6] L.Guo , M. Kondo, M. Fukawa, K. Saitoh, and A. Masuda, Jpn. J. Appl. Phys., Part 2 37, L1116 (1998)

[7] O. Vetterl et al., Sol. Energy Mater. Sol. Cells **62**, 97 (2000)

[8] J. Cifre, J. Bertomeu, J. Puigdollers, M. Polo, J. Andreu, and A. Lloret, Appl. Phys. A: Solids Surf. A59, 645 (1994)

[9] R. E. I. Schropp, Y. Xu, E. Iwaniczko, Z. A. Zaharias, and A. H. Mahan, Appl. Phys. A: Mater. Sci. Process. 715, A26.3 (2002)

[10] S. Klein, F. Finger and R. Carius, J. Appl. Phys. **98**, 024905 (2005)

[11] H. Matsumura, A. Masuda and H. Umemoto, Thin Solid Films **501**, (2006) 58-60

[12] A. Masuda, et. al., Japan. J. Appl. Phys. **25**, 54 (1986)

[13] A. Gallagher, J. Appl. Phys. **63**, 2406 (1988)

[14] J. Perrin, et. al., J. Vac. Sci. and Tech. **A16**, 278 (1998)

[15] J. Robertson, J. Non-Cryst. Solids **266-269**, 79 (2000)

[16] V.L. Dalal, Thin Solid Films **395** (2001) 173

[17] S. Miyazaki, N. Fukuhara and M. Hirose, J. Non-Cryst. Solids **266** (2000), 59

[18] V.L. Dalal, T. Maxson et al., J. Non-Cryst. Solids **227-230** (1998) 1257.

www.manaraa.com

[19] N. H. Nickel and W. B. Jackson, Phys. Rev. B **51**, 4872 (1995)

[20] A. Fontcuberta i Morral, J. Bertomeu, P. Roca i Cabarrocas, Mater. Sci. Eng. B69-70 (2000) 559-563

[21] S. Sriraman, S. Agarwal, E. S. Aydil and D. Maroudas, Nature **418**, 62-65 (2002)

[22] R.W. Collins, A.S. Ferlanto, G.M. Ferrerira., C. Chen, J. Koh, R. Koval, Y. Lee, J. Pearce, C. Wronski, Sol. Energy Mater. Sol. Cells **78**, (2003) 143–180

[23] D.H. Levi, B.P. Nelson, E. Iwanizcko and C.W. Teplin, Thin Solid Films **455 –456,** (2004) 679–683

[24] H. Takakura and Y. Hamakawa, , Sol. Energy Mater. Sol. Cells **74** (2002), 479-487

[25] H. Keppner et al., Appl. Phys. A: Solids Surf. **69**, 169 (1999)

[26] R. Biswas and B. C. Pan, NCPV and Solar Panel Review Meeting, 803-805 (2003)

[27] B.C. Pan and R. Biswas, J. Appl. Phys., **96**, 6247 (2004)

[28] F. Liu, M. Zhu, Y. Feng, Y. Han, J. Liu, Thin Solid Films **395**, (2001) 97–100

[29] S. Klein, F. Finger, R. Carius, H. Wagner and M. Stutzmann, Thin Solid Films **395**, 305 (2001)

[30] R. E. I. Schropp, Thin Solid Films **395**, 17 (2001)

[31] S. Klein, F. Finger and R. Carius J. Appl. Phys. **98**, 024905 (2005)

[32] C. Niikura, J. Guillet, R. Brenot, B. Equer, J.E. Bouree, C. Voz, D. Peiro, J.M. Asensi, J. Bertomeu, J. Andreu, J. Non-Cryst. Solids **266-269**, (2000) 385-390

[33] J. Lossen, S. Klein and F. Finger, Thin Solid Films **451-452,** (2004), 531-535

[34] J. Gu, M. Zhu, L. Wang, F. Liu, B. Zhou and Y. Zhou, J. Appl. Phys. **98,** 093505 (2005)

[35] R.E.I. Schropp, Thin Solid Films **451 –452,** (2004) 455–465

[36] S. Morrison and A. Madan, IEEE, 837-840 (2000)

[37] M. Fonrodona, D. Soler, J.M. Asensi, J. Bertomeu, J. Andreu, J. Non-Cryst. Solids **299–302**, (2002) 14–19

www.manaraa.com

[38] Wiesmann H., Ghosh A.K., McMahon T., Strongin M., J. Appl. Phys. 3752 (1979)

[39] Matsumura H., Jpn. J. Appl. Phys. 1522 (1991)

[40] A. Gallagher, Thin Solid Films **395,** (2001) 25-28

[41] M. Kondo, H. Fujiwara and A. Matsuda, Thin Solid Films **430**, (2003) 130-134

[42] H. L. Duan, G. A. Zaharias, and Stacey F. Bent, Appl. Phys. Lett. **78**, 1784 (2001)

[43] E. C. Molenbroek, A. H. Mahan, A. Gallagher, J. Appl. Phys. **82**, 1909 (1997)

[44] S. Nakamura, M. Koshi, Thin Solid Films **501**, (2006) 26-30

[45] H. Matsumura et al., J. Non-Cryst. Solids **338–340**, (2004) 19–26

[46] S. Klein, T. Repmann, T. Brammer, Sol. Energy Mater. Sol. Cells **77,** (2004) 893–908

[47] M. Kupich, D. Grunsky, P. Kumar, B. SchrÖder, Sol. Energy Mater. Sol. Cells **81**, (2004) 141–146

[48] J.J.H. Strengers, F.A. Rubinelli, J.K. Rath, R.E.I. Schropp, Thin Solid Films **501**, (2006) 291-294

[49] H. Li , R.L. Stolk, C.H.M. van der Werf, M.Y.S. Rusche, J.K. Rath, R.E.I. Schropp, Thin Solid Films **501,** (2006) 276-279

[50] S. DeBoer, Ph. D Thesis, Iowa State University, 1995

[51] E. Bustarret, M. A. Hachicha, M. Brunel, Appl. Phys. Lett. **52**, 1675 (1988)

[52] B.D. Cullity, Elements of X-ray diffraction, Addison-Wesley Publishing Company, Inc. Boston, MA (1978) 101-102

[53] L. C. Kimerling, J. Appl. Phys. **45,** (1974) 1839-1845

[54] V. Dalal , P. Sharma, Appl. Phys. Lett. **86,** (2005) 103510

[55] V. Dalal, P. Sharma, et al. Mat. Res. Soc. Symp. Proc. **808** A 8.2, (2004) 64-71

[56] M. Pontoh, M. S Thesis, Iowa State University (2002)

[57] V. L. Dalal, K. Muthukrishnan, D. Stieler and M. Noack, Mater. Res. Soc. Symp. Proc. **862**, 69 (2005)

[58] R. J. Jaccodine, J. Electrochem. Soc. **110**, 1963, 524-527

www.manaraa.com

[59] M. I. Jones, I. R. McCall, D. M. Grant, Surf. Coat. Technol. **132** (2000) 143-151

[60] V. L. Dalal, K. Muthukrishnan, X. Niu and D. Stieler, J. Non-Cryst. Solids **352**, (2006) 892–895

[61] S. Veprek, Mat. Res. Soc. Symp. Proc. **164**, 39 (1990)

[62] M. Heintze and S. Veprek, Appl. Phys. Lett. **54**, 1320 (1989)

[63] S. Veprek and M. G. J. Veprek-Heijman, Appl. Phys. Lett, **56**, 1766 (1990)

www.manaraa.com